Dynamical Analysis of Extreme Precipitation in the US Northeast Based on Large-scale Meteorological Patterns

[1]Laurie Agel[a,b,*], [1]Mathew Barlow[a,c], Frank Colby[a], [2]Hanin Binder[d,e], Jennifer L. Catto[f], Andrew Hoell[g], [3]Judah Cohen[h]

[a]Department of Environmental, Earth, and Atmospheric Sciences, University of Massachusetts Lowell, Lowell, MA, USA

[b]Intercampus Marine Science Graduate Program, University of Massachusetts Lowell, Lowell, MA, USA

[c]Climate Change Initiative, University of Massachusetts Lowell, Lowell, MA, USA

[d]Institute for Atmospheric and Climate Science, ETH Zurich, Zurich, Switzerland

[e]Laboratoire de Météorologie Dynamique / IPSL, École Normale Supérieure, Paris, France

[f]College of Engineering, Mathematics and Physical Sciences, University of Exeter, UK

[g]NOAA/ESRL Physical Sciences Division, Boulder, CO

[h]Atmospheric and Environmental Research, Lexington, USA

[1]*Funding provided by National Science Foundation (NSF Project #1623912)*

[2]*HB is supported by the Swiss National Science Foundation (SNSF) via grant 200020_146834/P2EZP2_175161*

[3]*JC is supported by the National Science Foundation Division of Polar Programs (grant PLR-1504361) and the National Science Foundation Large-Scale and Climate Dynamics Program (grants AGS-1657748).*

*Corresponding Author: Laurie Agel, Dept. of Environmental, Earth, and Atmospheric Sciences, University of Massachusetts Lowell, One University Avenue, Lowell, MA 01854, Email: lagel48@gmail.com

Abstract

Previous work has identified six Large-Scale Meteorological Patterns (LSMPs) of dynamic tropopause height associated with extreme precipitation over the Northeast US, with extreme precipitation defined as the top one percent of daily station precipitation. Here, we examine the three-dimensional structure of the tropopause LSMPs in terms of circulation and factors relevant to precipitation, including moisture, stability, and synoptic mechanisms associated with lifting. Within each pattern, the link between the different factors and extreme precipitation is further investigated by comparing the relative strength of the factors between days with and without the occurrence of extreme precipitation.

The six tropopause LSMPs include two ridge patterns, two eastern US troughs, and two troughs centered over the Ohio Valley, with a strong seasonality associated with each pattern. Extreme precipitation in the ridge patterns is associated with both convective mechanisms (instability combined with moisture transport from the Great Lakes and Western Atlantic) and synoptic forcing related to Great Lakes storm tracks and embedded shortwaves. Extreme precipitation associated with eastern US troughs involves intense southerly moisture transport and strong quasi-geostrophic forcing of vertical velocity. Ohio Valley troughs are associated with warm fronts and intense warm conveyor belts that deliver large amounts of moisture ahead of storms, but little direct quasi-geostrophic forcing. Factors that show the largest difference between days with and without extreme precipitation include integrated moisture transport, low-level moisture convergence, warm conveyor belts, and quasi-geostrophic forcing, with the relative importance varying between patterns.

1 Introduction

Extreme precipitation is responsible for some of the most destructive and costly, in terms of human lives and resources, natural disasters in the Northeast US (Kunkel et al. 2013). These disasters include localized flash flooding in streams due to summertime convective events, urban flooding due to extreme rainfall and poor drainage, and widespread river flooding due to tropical cyclones and spring rains combined with snowmelt. Unfortunately, the vulnerability of this region to the effects of extreme precipitation is expected to grow, as 99th-percentile daily precipitation in the region has increased 74% from 1958–2010 (Groisman et al. 2013), while future winter and spring precipitation over this region, based on a range of model projections using the A2 emissions scenario, is expected to increase between 5–20% by the end of this century (Melillo et al. 2014). The goal of this study is to investigate the dynamical mechanisms and moisture ingredients associated with Northeast US (hereafter "Northeast") extreme precipitation by building on previous work that identifies several large-scale circulation patterns associated with this extreme precipitation (Agel et al. 2017), and providing a first step toward being able to accurately predict and prepare for future precipitation challenges for the region.

The mechanisms by which precipitation is delivered to the Northeast depend upon location relative to the coastline. Precipitation in the coastal region is strongly influenced by extratropical storms traveling along the high-density North Atlantic storm track (Hoskins and Hodges 2002). Precipitation in the inland region, while influenced by the North Atlantic storm track as well as extratropical storms traveling across the Great Lakes region, is also orographically influenced by the Adirondack, Green, and White Mountain ranges. These different regional influences result in fewer precipitation days at coastal stations than at inland stations, but with considerably higher daily intensity at coastal stations (Agel et al. 2015). At

inland stations the highest daily intensity occurs in warm months, while at coastal stations peaks in daily intensity occur in spring and fall. Extreme daily precipitation (based on top 1% daily station precipitation) varies from 30+ mm at inland locations to 70+ mm at coastal locations. For both inland and coastal locations, extreme precipitation days tend to occur embedded within multiple-day precipitation events.

Accordingly, a complete dynamical analysis of extreme precipitation in the Northeast needs to consider both synoptic-scale influences as they apply to the entire region, as well as localized and sub-regional responses to those larger-scale influences. Several researchers, as part of larger-domain or global studies, have addressed the first issue by evaluating the role of synoptic-scale influences on extreme precipitation in the Northeast. Pfahl and Wernli (2012), using 99th percentile 6-hourly modeled precipitation, estimated that 60–80% of extreme precipitation along the eastern US seaboard occurs near extratropical cyclone centers. Pfahl and Sprenger (2016) quantified the role of cyclone intensity and moisture availability in generating precipitation, and found that intensity and moisture scale well to precipitation, especially in low-latitudes, but that moisture availability can act as an independent factor in mid- and high-latitudes. Collow et al. (2016) found strong anomalous moisture transport and lower sea level pressure associated with summertime Northeast cyclones for 95th percentile precipitation events. Kunkel et al. (2012), using daily precipitation exceeding a 1-in-5-year occurrence, found that Northeast extreme precipitation can be attributed in 16% of the cases to nearby extratropical cyclones, in 47% of the cases to frontal processes, and in 36% of the cases to tropical cyclones. Dowdy and Catto (2017) found that the combination of a cyclone and a front is the most common cause of extreme precipitation (6-hourly 99th percentile) in the Northeast.

Several studies have further explored the relevance of fronts to precipitation. Based on global figures from Catto et al. (2012), approximately 18-30% of Northeast annual total daily precipitation is related to cold fronts, while 30-42% is related to warm fronts. However, extreme precipitation is more likely to be associated with warm fronts: Catto and Pfahl (2013) found that 40-50% of 6-hourly ERA-Interim extreme precipitation occurs with nearby warm fronts in the Northeast, despite the fact that only 5-10% of fronts generate extreme precipitation.

Warm conveyor belts (WCBs), well-defined moist airstreams in an extratropical cyclone's warm sector that rise from the boundary layer into the upper troposphere (Green et al. 1966, Harrold 1973, Wernli and Davies 1997) and feature intense latent heat release (Browning 1990), are also linked to extreme precipitation. For the eastern US, Pfahl et al. (2014) showed that about 50-70% of all extreme precipitation events between 1979 and 2010 were related to WCBs. WCBs, particularly those linked to extreme precipitation, often occur in conjunction with warm and cold fronts in the Northeast (Catto et al. 2015). WCBs also play an important role for atmospheric dynamics. In the early phase of the WCB ascent, diabatic potential vorticity (PV) production leads to the formation of a positive PV anomaly (Wernli and Davies 1997), which is essential for the intensification of many strongly deepening cyclones (Stoelinga 1996; Binder et al. 2016), while in the upper troposphere diabatic PV reduction produces negative PV anomalies that can amplify upper-level ridges and influence the downstream flow evolution (Wernli 1997, Pomroy and Thorpe 2000, Grams et al. 2011).

In the current study, we build on these previous results, while also examining the sub-regional response to larger-scale synoptic forcings, by taking a detailed view of the processes related to extreme Northeast precipitation within the context of several Large-Scale Meteorological Patterns (LSMPs; Grotjahn et al. 2016). LSMPs are typically defined at a scale

larger than the mesoscale but smaller than the scale of climate variability, and relate to some observed phenomena, such as precipitation or temperature extremes (e.g., Loikeith and Broccoli 2012, Glisan and Gutowski 2014, Callow et al. 2016, Roller et al. 2016). Here, the LSMPs used are six previously-defined upper-level circulation patterns of dynamic tropopause height that are linked to the top 1% of daily extreme precipitation in the Northeast (Agel et al. 2017). Dynamic tropopause height is an effective field to use for large-scale pattern identification, since it provides a compact representation of the upper-level flow, as gradients of PV along the tropopause are directly related to the strength of upper-level troughs and ridges (Hoskins et al. 1985, Nielson-Gammon 2001). For each tropopause LSMP, we examine the associated three-dimensional large-scale circulation, as well as a range of factors relevant to precipitation, including moisture, stability, and synoptic mechanisms associated with lifting. Because the six LSMPs are linked to extreme precipitation days only, we extend our analysis by also considering six similar patterns drawn from a set of LSMPs identified for all days 1979–2008 (Agel et al. 2017). For the similar-patterned LSMPs, we compare the relative strength of the circulation and factors between days with and without the occurrence of extreme precipitation.

The paper is organized as follows. In Section 2, the data products and methods used to develop the tropopause patterns and to identify the key ingredients or processes related to extreme precipitation within each tropopause pattern are described. In Section 3, the tropopause LSMPs are described and a set of composite figures showing key circulation fields, moisture fields, instability measures, and synoptic mechanisms for each set of pattern days, as well as the differences between several of these fields on extreme vs. non-extreme days, are used to examine how these factors relate to extreme precipitation within each LSMP. In Section 4 we provide a summary of our results (including a summary schematic of how circulation, moisture, and

instability contribute to extreme precipitation within each of our tropopause patterns), as well as further discussion regarding the role of moisture transport, and a brief discussion of future work.

2 Data and Methods

2.1 Extreme precipitation days

Northeast extreme precipitation is identified as the top 1% of daily precipitation exceeding 0.01 in, or 0.254 mm, at 35 United States Historical Climatology Network (USHCN; Easterling et al. 1999) stations for the years 1979–2008, as developed in Agel et al. (2015). Each station is missing no more than 1% of the daily values. Extreme days related to tropical cyclones, defined as days where a station experiencing extreme precipitation is within 1000 km of a HURDAT2 (Landsea and Franklin 2013) tropical cyclone track, are eliminated, leaving a total of 691 unique dates with non-tropical cyclone-related extreme precipitation at one or more stations. The station locations, regional variation of top 1% threshold values, and seasonal frequency of the extreme dataset are shown in Online Resource 1, reproduced from Agel et al. (2015), where the division of coastal and inland stations runs roughly along the 45 mm day^{-1} threshold contour. The seasonal categories used here and throughout the paper are December–February (DJF), March–April (MAM), June–August (JJA), and September–November (SON). The National Oceanic and Atmospheric Administration (NOAA) Climate Prediction Center (CPC) 0.25° x 0.25° Daily U.S. Unified Precipitation (CPCU; Chen et al. 2008) is also used to show region-wide precipitation, and is provided by NOAA/OAR/ESRL PSD (http://www.esrl.noaa.gov/psd/http://www.esrl.noaa.gov/psd/data/gridded/data.unified.daily.conus.html).

2.2 Dynamic tropopause patterns

159 The six tropopause LSMPs, previously identified in Agel et al. (2017), are created by
160 applying k-means clustering (KMC; Diday and Simon 1976, Michelangeli et al. 1995) to daily
161 standardized anomalies of dynamic tropopause height for the 691 extreme precipitation days
162 defined above. The standardized anomaly fields are created from daily means of the National
163 Aeronautics and Space Administration (NASA) Modern Era Retrospective Reanalysis for
164 Research and Application (MERRA, Rienecker et al. 2011) blended tropopause height (provided
165 in units of pressure, at 1-hourly intervals on a 2/3° x 1/2° grid). This field is a smoothed mix of
166 PV-based tropopause pressure at higher latitudes and temperature-based tropopause pressure at
167 lower latitudes. Because we use MERRA's blended approach to defining the tropopause height,
168 we use the terms "dynamic tropopause height" and "tropopause pressure" interchangeably here.
169 The standardized anomalies are produced by removing the long-term daily mean from the daily
170 mean at each grid point, and dividing the result by the temporal standard deviation of the values
171 at the grid point. The long-term daily mean is created at each grid point by taking a 30-year mean
172 of each calendar day and smoothing the results with a 21-day running mean.
173 In addition to KMC typing on extreme precipitation days, Self-Organizing Maps (SOMs,
174 Kohonen 2001) of dynamic tropopause height for all days 1979–2008, previously developed in
175 Agel et al. (2017), are used to identify the differences between extreme precipitation days and
176 non-extreme precipitation days within each SOM pattern. The SOM technique applies
177 unsupervised learning to neural network classifications, to create a number of distinct "nodes",
178 or patterns, for an input field. Here, the input field is identical to the dynamic tropopause height
179 field used for the KMC analysis, and the SOM algorithm is specified to use linear initialization,
180 200 initial training iterations, 1200 secondary training iterations, and a 5 x 6 rectangular pattern

space with an initial training radius of 6. A complete description of the KMC and SOM methods used to create the tropopause LSMPs is available in Agel et al. (2017).

2.3 Additional reanalysis variables

We use additional MERRA reanalysis data to evaluate the key dynamical fields and physical properties associated with the extreme precipitation-producing circulation patterns. 200-hPa winds, 500-hPa geopotential heights, mean sea level pressure (MSLP), and 700-hPa vertical velocities are used to identify the three-dimensional circulation associated with each LSMP. Lowest model level winds and specific humidity are used to show low-level moisture convergence (LLMC), which can enhance precipitation amounts above that expected from a simple Clausius-Clapeyron perspective (Muller et al. 2011). Integrated vapor transport (IVT) is used to provide a measure of moisture flux into the region. The static stability parameter for an isobaric system, calculated at 750 hPa from temperature and pressure per Eq. 3.7 in Holton (2004), is used to show areas where buoyancy can enhance precipitation production. Ertel's PV (EPV), for the 900–100-hPa layer, is used to show vertical cross-sections where lift may be enhanced by diabatic heating, particularly due to the release of latent heat during precipitation. The thermal wind form of quasi-geostrophic (QG) forcing (right-hand-side of Eq. 6.36 in Holton 2004), specifically the advection of 700-hPa geostrophic relative vorticity by the 900–500 hPa thermal wind[1], is used to identify areas where synoptic mechanisms such as temperature advection and vorticity advection may play a role in generating lift. The MERRA data is at two different resolutions – geopotential heights, temperature, MSLP, horizontal winds, EPV, specific humidity, and vertical velocity are provided at 3-hourly intervals on a 1.25° x 1.25° grid; while

[1] The 900–500 hPa layer is chosen as opposed to the more familiar 1000–500 hPa layer because MERRA does not include interpolated values below the lowest model sigma level, resulting in many missing values at 1000 hPa for the Northeast.

202 IVT and other single-level fields are available at 1-hourly intervals on a 2/3° x 1/2° grid. Unless
203 otherwise noted, the MERRA data is evaluated at 12 UTC.
204 Convective Available Potential Energy (CAPE) from NOAA's National Centers for
205 Climate Prediction (NCEP) Climate Forecasting System Reanalysis (CFSR; Saha et al. 2010), a
206 high-resolution coupled atmosphere-ocean-land surface-sea ice system, is used to show regions
207 of potential convection[2]. The field is available at 6-hour intervals on a 0.5° x 0.5° grid. Here we
208 use the 18 UTC field, as CAPE values for the Northeast tend to peak from 18–22 UTC (based on
209 manual inspection for the dates considered).
210 Anomalies of all reanalysis fields are calculated by subtracting the smoothed long-term
211 daily means at each grid point from the 12 UTC (unless otherwise noted) fields. The long-term
212 daily means are calculated as for MERRA tropopause height.
213 **2.4 Storm tracks**
214 Storm track data is derived by applying the tracking algorithm of Hoskins and Hodges
215 (2002) to 6-hourly European Center for Medium-range Weather Forecasting (ECMWF) ERA-
216 Interim (Dee et al. 2011) 850-hPa relative vorticity with a methodology similar to Catto et al.
217 (2010). The vorticity field is spectrally truncated at 42 wavenumbers (T42) to eliminate small-
218 scale features, and further filtered to remove wavenumbers n<=5 before identification of
219 vorticity maxima. Tracks are established from the maxima using a nearest neighbor approach,
220 from which the smoothest set of tracks, based on minimizing a cost function, are selected. The
221 tracks are further filtered to those with duration of at least 2 days and propagation distance of at
222 least 1000 km.

[2] The CFSR CAPE field is used instead of calculation directly from MERRA due to the lack of MERRA interpolated values below 900 hPa for the Northeast.

223 The storm track data is used to identify extreme station precipitation as storm-related
224 (non-storm-related) if the station experiencing precipitation is within (outside of) 800 km of a
225 storm center on the day of precipitation. The 800-km threshold is based on a manual review of
226 station precipitation and nearby storm tracks, and is used to capture the majority of storm-related
227 dynamics, but does not necessarily include precipitation related to elongated fronts far removed
228 from storm centers, or that due to other mechanisms such as localized convection and mesoscale
229 convective complexes (MCCs).

230 **2.5 Fronts**

231 Cold and warm fronts are identical to those used in Catto et al. (2012), Catto and Pfahl
232 (2013), and Catto et al. (2014). The fronts are derived from ECMWF ERA-Interim reanalysis,
233 using an objective identification algorithm from Berry et al. (2011) to identify organized
234 locations where a selected thermal front parameter (based on 850 hPa wet bulb potential
235 temperature) is lower than a specified negative threshold value. Fronts are then placed where the
236 gradient of the thermal front parameter is zero (Hewson 1998). The fronts are identified as warm
237 or cold based on overall speed and direction, and are provided on a 2.5° x 2.5° grid at 6-hour
238 intervals.

239 Frontal density at each grid box is calculated per day based on the number of times a
240 front is present in each grid box (0-4 counts per day). The densities are calculated in a station-
241 relative manner (that is, the front positions are shown in relation to the location of the stations
242 experiencing extremes). In this case, for each extreme precipitation day (which may feature
243 extreme precipitation at more than one station), the nearest frontal grid location is found for each
244 station experiencing extreme precipitation, and a surrounding 35° latitude x 40° longitude box
245 (with the station in the center) is used to gather the station-relative frontal density. Station-centric

246 frontal density on an extreme day is then calculated as the mean of these 35° x 40° station-
247 relative frontal densities. In addition, Online Resource 2 shows the actual composite location of
248 the fronts for storm-related and non-storm-related days, as well as the station-centric warm and
249 cold fronts separated by coastal and inland station extremes.

250 **2.6 Warm Conveyor Belts**

251 WCBs are obtained from the global climatology of Madonna et al. (2014), based on 6-
252 hourly ECMWF ERA-Interim reanalysis fields evaluated at 60 vertical levels and interpolated
253 onto a 1° x 1° longitude-latitude grid. WCB trajectories are calculated with the trajectory tool
254 LAGRANTO (Wernli and Davies 1997; Sprenger and Wernli 2015). At each 6-hourly time step,
255 three-dimensional kinematic two-day forward trajectories are started from an equidistant grid in
256 the lower troposphere (between 1050 and 790 hPa) with a horizontal spacing of 80 km and a
257 vertical spacing of 20 hPa. Trajectories that ascend more than 600 hPa within two days in the
258 vicinity of an extratropical cyclone are then classified as WCB trajectories (see Madonna et al.
259 2014 for details). Analogous to Binder et al. (2016), low- and upper-level WCB trajectory
260 frequencies are defined at each grid point as the percentage of pattern days associated with at
261 least one WCB air parcel with $p > 500$ hPa and $p < 500$ hPa, respectively, at the grid point at 12
262 UTC.

263 **2.7 Statistical significance**

264 Statistical significance, unless noted otherwise, is established through a Monte Carlo
265 approach, in which the pattern assignments are randomly shuffled (among the 691 days for the
266 KMC clusters, or among all days for the SOM patterns), and the desired quantity (for example,
267 seasonal frequency of the KMC pattern dates) is recalculated. This process is repeated 1000

268 times, creating a range of values. A quantity is considered statistically significant if it falls below
269 the bottom 2.5% or above the top 97.5% of the randomly generated values.

270 **2.8 Comparison of fields between extreme and non-extreme days**

271 Differences between extreme-precipitation days and non-extreme precipitation days
272 within each LSMP are explored for select fields using the all-days SOM patterns most similar to
273 the KMC patterns. To identify these differences, each of the KMC patterns must also occur in the
274 all-day SOM context, and the SOM patterns most similar to the KMC patterns must explain the
275 majority of extreme precipitation. Online Resource 3, reproduced from Agel et al. (2017), shows
276 the tropopause SOM patterns, the frequency of extreme precipitation days represented by each
277 SOM pattern, and the frequency of KMC pattern days C1–C6 represented by each SOM pattern.
278 The SOM patterns most representative of the C1–C6 patterns and used in this paper are SOM4,
279 SOM26, SOM13, SOM8, SOM20, and SOM1, respectively.

280 For each field, the non-extreme-day composite is subtracted from the extreme-day
281 composite, and the results are standardized at each grid point by subtracting the grid point mean
282 and dividing by the grid point temporal standard deviation. This allows a comparison of the
283 relative strength of the fields' differences, independent of the units of the original fields. Only
284 statistically significant differences at the 0.05 level as defined through Monte Carlo resampling
285 are considered.

286 **3 Results**

287 The six tropopause LSMPs (Agel et al. 2017) are reproduced here in Fig. 1a, along with
288 the seasonal frequency of the patterns (Fig 1b), and the location of precipitation and extreme
289 precipitation events within each pattern (Fig 1c). The patterns represent three basic tropopause
290 configurations: a ridge over the Northeast, a trough along the eastern US, and a trough over the

Ohio Valley. The six-pattern set of LSMPs includes two distinct ridge patterns (C1 and C4, together representing over 44% of the extremes), two seasonal variations of the eastern trough (C2 and C5), and two seasonal variations of the Ohio Valley trough (C3 and C6). The remainder of this section will address each of the ridge patterns separately, followed by an analysis of the eastern troughs together, and finally an analysis of the Ohio Valley troughs together.

3.1 Ridge pattern C1

The C1 pattern features an anomalously high tropopause ridge spread across the eastern US (Fig. 1a). Although extreme precipitation can occur anywhere in this pattern, it occurs most often along the Canadian/New England border during JJA (Fig. 1b,c). However, overall precipitation is light, suggesting localized processes for extreme precipitation. The pattern is associated with predominantly westerly flow at mid- and upper-levels (Fig. 2a,b) and widespread anomalously low MSLP to the west of the region (Fig. 2c). There is widespread slightly anomalous upward motion (approximately -0.5 Pa s^{-1}, consistent through a deep layer of the air column) at grid scale (Fig. 2d). There are regions with low-level moisture convergence (LLMC) anomalies, particularly to the northwest along the Great Lakes (Fig. 2e), and anomalously high IVT values extending from the Ohio Valley into the interior Northeast (Fig. 2f). These anomalies are often in place at least 48 hours before extreme precipitation occurs (not shown). Static stability (Fig. 2g) is anomalously low for the entire pattern, but is especially low in western New York, where LLMC and IVT are largest. The warm moist air mass and weak synoptic-scale forcing suggests that convection plays an important role in extreme precipitation production for this pattern. This is supported by the CAPE anomalies in Fig. 2h, which are the highest and most widespread of the six patterns for the Northeast region.

313 While organized convection is likely a key factor in these extremes, a more complex
314 situation is revealed when nearness to storm tracks and surface fronts are explored. Although the
315 storm track density is the weakest of the six patterns, and, accordingly, the percent of storm-
316 related extremes is the lowest for the six patterns (Table 1), still more than 70% of the extremes
317 in this pattern are storm-related, suggesting the important role of synoptic-scale triggering of
318 mesoscale processes. However, anomalies for storm-related fields, such as QG forcing (Fig. 2i),
319 WCBs (Fig. 2j), and EPV (Fig. 2k) are very small, indicating that storms in this pattern are likely
320 weak and shallow.
321 For both storm-related and non-storm-related extremes, warm fronts tend to be located
322 nearby (Fig. 2l). Cold fronts also appear nearby to stations experiencing non-storm-related
323 extremes. These cold fronts may be associated with distant storm centers, or they may be surface
324 fronts caused by other mechanisms such as cold pools and mesoscale convective system
325 outflows (Schumacher and Johnson 2005). The frontal patterns may also be consistent with small
326 frontal-wave cyclones spinning up on trailing cold fronts, which could explain the presence of
327 cold fronts to the northeast of the stations and the high frequency of warm fronts in the non-
328 storm related composites.
329 Thermal fronts can be initiated by shortwaves passing through a ridge environment. Fig.
330 2c shows a composite "kink" in the MSLP over the Great Lakes, which could reflect a surface
331 response to shortwaves. Although the composite 500-hPa heights do not show this, many of the
332 individual 500-hPa height maps do show evidence of shortwaves in the overall flow. This is
333 consistent with the findings of Milrad et al. (2014), who found that vorticity maxima propagating
334 through longwave ridges often provided a warm-season trigger for convection in Montreal. The
335 presence of anomalous LLMC in western New York may also provide some evidence of

shortwave activity and attendant surface circulation. In Fig. 3 we composite station-relative MERRA 500-hPa geopotential heights for the C1 pattern on the higher-resolution 2/3° x 1/2° grid, separated into storm-related and non-storm-related extremes. There is a noticeable shortwave in the composite pattern for storm-related extremes, along with an area of positive relative vorticity, which is not present for the non-storm-related extremes, confirming that at least some of the precipitation extremes in this pattern may be related to shortwaves and their attendant surface disturbances.

Many of the circulation features and moisture variables in this pattern occur on non-extreme precipitation days as well, based on similar patterns in the all-day SOM analysis. However, the ingredients most important for generating extreme precipitation as opposed to ordinary precipitation in the C1 pattern include surface lows (possibly due to shortwaves) over western New York (Fig. 4b), moisture availability due to strong southwesterly IVT and LLMC (Fig. 4c,d), and convection in regions of relatively high CAPE (Fig. 4f).

3.2 Ridge/trough C4

Like C1, the C4 pattern features an anomalously high tropopause ridge over the Northeast, but unlike C1, the C4 ridge is part of a shallow tropopause ridge/trough couplet located across the eastern US (Fig. 1a). This pattern is also similar to C1 in seasonality (mostly JJA; Fig. 1b), precipitation features (widespread light precipitation), and location of extremes (more extremes inland and to the northwest; Fig. 1c). Upper- and mid-level circulation fields (Fig. 5a,b) also mirror the tropopause trough/ridge, with a widespread area of anomalously low MSLP (Fig. 5c) across the Northeast. There is slightly more upward vertical motion (Fig. 5d) than for pure ridge C1, possibly aided by a 200-hPa jet streak over northern New England, but overall upward motion is not particularly extreme, except in localized pockets. Surface heating is

strong over coastal regions, with a thermal boundary along northern and western New England separating cooler air to the north (not shown). Despite extremes occurring more frequently inland, localized pockets of heavy precipitation also occur along the coast, where moderate moisture availability, in terms of LLMC (Fig. 5e) and IVT (Fig. 5f), is present. Like C1, static stability is anomalously low (Fig. 5g), and convection appears to be associated with some of the extremes, particularly in New York (Fig. 5h).

QG forcing (Fig. 5i) is moderate over regions with high numbers of extremes (western New York), consistent with the enhanced frequency of inland storms (Table 1). Coastal regions contain areas of weak WCB density (Fig. 5j), and slightly elevated EPV at low levels (Fig. 5k). Cold and warm fronts are associated with both storm-related and non-storm-related extremes (Fig. 5l). This indicates that at least some of the storm-related extremes in coastal regions are linked to WCBs ascending over the warm or cold fronts of the associated storms. Otherwise the pattern is consistent with relatively weak synoptic systems at inland locations, or trailing cold fronts associated with remote cyclones to the northeast. The key factors linked to extreme precipitation in this pattern, as opposed to ordinary precipitation, are enhanced moisture transport due to IVT and LLMC along the coast (Fig. 6c,d), the presence of WCBs near the coast (Fig. 6e), and slightly elevated CAPE in southern regions (Fig. 6f).

3.3 Eastern troughs C2 and C5

The C2 and C5 patterns feature tropospheric troughs across the eastern US. The C2 trough axis extends from the Great Lakes through the Carolinas, with a slight negative tilt and a closed or nearly closed upper-level low (Fig. 1a). The C5 pattern is both shallower and shifted slightly farther east than C2, and unlike C2, features a slight progressive tilt (Fig. 1a). The C2 pattern occurs preferentially during DJF and MAM, while the C5 pattern occurs preferentially

during JJA (Fig. 1b). Unlike the other patterns, the stations experiencing the highest number of extremes in these patterns are located along the eastern seaboard – to the extreme southeast for C2, and in Maine for C5 (Fig. 1c). The composite daily precipitation intensity in C2 is the strongest of the patterns (71.2 mm day^{-1}).

Over 90% of the extreme days in C2 are associated with nearby storms (Table 1), with roughly 2/3 of the storm-related extremes occurring at coastal stations. Composite circulation shows an absence of jet streaks (Fig. 7a), a nearly closed mid-level circulation with a slightly regressive tilt (Fig. 7b), and a well-defined surface low with central pressure that is the lowest of the six patterns (Fig. 7c). There is a strong thermal gradient between an anomalously cool Ohio Valley and an anomalously warm Northeast (not shown). Upward motion anomalies are among the highest of the patterns (Fig. 7d), peaking at nearly -1.0 Pa s^{-1} around 750 hPa. The pattern also features strong coastal LLMC (Fig. 7e), along with enhanced south-southeast moisture transport over the relatively warm Western Atlantic (Fig. 7f), beginning up to 48 hours before the extreme event. Overall static stability is very low along the immediate coast (Fig. 7g), but CAPE is not anomalously high (Fig. 7h). Consequently, QG forcing appears to be the dominant mechanism in C2 for lift, and is in fact the strongest of the six patterns (Fig. 7i). There is also relatively frequent WCB ascent (Fig. 7j) at the upstream edge of the upper-level disturbance (although this is mostly located offshore). EPV is enhanced at low levels in the regions experiencing extreme precipitation (Fig. 7k), indicating that diabatic heating may provide a positive feedback mechanism for additional lift in this pattern. For storm-related extremes, the most frequent frontal mechanism for lift appears to be attendant warm fronts (Fig. 7l). Based on the above composite features, the C2 pattern is consistent with many of the features of traditional nor'easters (Maglaras et al. 1995, Kocin and Uccellini 2004), unusually strong storms that form

405 along the Mid-Atlantic coastline and travel north through or near to New England along a dense
406 track location off the New Jersey/Southern New England coast.
407 For the summertime C5 pattern, mid- and upper-level circulation is more open and
408 progressive than for the wintertime C2 pattern (Fig. 8a,b). Like C2, the extremes in this pattern
409 have a high likelihood to be storm-related (Table 1). The composite surface low is located along
410 the Maine coast (Fig. 8c), where the highest-intensity precipitation occurs (Fig. 1c). Storms in
411 this pattern tend to track from southern Ontario towards southeastern New England before
412 moving northeast through Maine (not shown). Lift is noticeably weaker in this pattern than for
413 C2 (Fig. 8d), except along the Maine coast. This is a rather dry pattern throughout the rest of the
414 region, as the anomalous moisture flow for both LLMC and IVT is from the north (Fig. 8e,f).
415 However, there is weak instability (Fig. 8g), and slightly enhanced CAPE at inland locations
416 (Fig. 8h). In addition, there is moderate QG forcing throughout the region (Fig. 8i), but only
417 weak WCB frequency located offshore (Fig. 8j), and no notable diabatic heating suggested by
418 the EPV cross-section (Fig. 8k). Fronts appear to be too far from station locations to provide
419 triggering mechanisms, except in the case of non-storm-related cold fronts (Fig. 8l), especially at
420 inland stations. In these cases, the cold fronts are located both to the southwest and northeast of
421 the station location, suggesting that some extremes may be related to remote cyclones with
422 trailing cold fronts. Hence in this pattern the inland extremes may be associated with both direct
423 QG forcing from weak storms and lift associated with trailing cold fronts; while the coastal
424 extremes may be associated with direct QG forcing by stronger storms, and possibly southerly
425 moisture transport in offshore WCBs and warm fronts.
426 Although C2 and C5 differ in some respects, the key elements that distinguish extreme
427 precipitation-producing days from non-extreme precipitation-producing days are very similar.

These include enhanced tropospheric ridging over southeastern Canada (Figs. 9a, 10a), a well-defined storm track with more intense storms (Figs. 9b, 10b), and stronger southerly moisture feed embedded in WCBs (Figs. 9d,e, 10d,e); but notably do not include enhanced QG forcing in the regions experiencing the highest number of extremes (Figs. 9f, 10f).

3.4 Ohio Valley troughs C3 and C6

The Ohio Valley trough patterns C3 and C6 represent the deepest tropopause troughs associated with Northeast extreme precipitation, with trough axes extending from the western Great Lakes through the southern US states. C3 represents the deepest troposphere trough (Fig. 1a), and is common in MAM and SON (Fig. 1b); while the C6 trough is both slightly shallower and shifted farther west than its C3 counterpart (Fig. 1a), and occurs preferentially in DJF (Fig. 1b). The C6 pattern, featuring the strongest ridging of the six patterns (concentrated over southeastern Canada), is the least frequent of the six patterns (only 9% of extreme precipitation days fall into this category). There is widespread anomalously intense precipitation over the entire region for C3, and over more southerly regions for C6 (Fig. 1c).

Large-scale circulation is similar for both patterns (but more pronounced for C6), with jet streaks over extreme northern New England (Figs. 11,12a), well-defined anomalous 500-hPa troughs and ridges (Figs. 11,12b), and surface lows tracking across inland portions of the eastern US (Figs. 11,12c). In general, however, the composite surface lows for C3 and C6 are not as deep as those for the C2 pattern. The Northeast is wedged between anomalously cold and warm air masses (not shown), and there is strong lift over the Northeast (Figs. 11,12d). Enhanced LLMC is concentrated along the southeast coast (Figs. 11,12e), and IVT (Figs. 11,12f) is the strongest of the patterns, with anomalously high values extending from the Florida coast into interior New England. QG forcing is present for western locations in C6 and throughout most of

451 the domain for C3 (Figs. 11,12i), but the forcing is weaker than that for C2 and C5. However, the
452 frequency of WCBs (Figs. 11,12j), especially for C6, is the highest of the patterns. In addition,
453 anomalously high EPV values are present throughout the cross section (Figs. 11,12k), hinting at
454 intense latent heating within the ascending WCB airstreams. Warm fronts are near to stations
455 experiencing extremes (Figs. 11,12l), for both storm-related and non-storm-related precipitation,
456 and at both inland and coastal stations. For non-storm-related extremes, cold fronts may also
457 accompany extremes, especially for inland locations.

458 Despite the cohesiveness of the WCB high-frequency locations in relation to the areas
459 experiencing extremes, there is no well-defined storm track, but rather a loose cluster of tracks
460 over the region for C3, and a smaller cluster of tracks to the south of New York and Connecticut
461 for C6 (not shown). This stands in sharp contrast to the C2 pattern, where most extremes feature
462 surface lows tracking in the same area along the eastern seaboard. Accordingly, extreme
463 precipitation in these patterns is likely linked, at least in part, to the strength (intensity of ascent)
464 of the WCBs, which are linked to the strong QG forcing to the west of the domain (where the
465 surface lows are positioned). Overall, although the C3 and C6 patterns share many similar
466 features, the higher intensity of the C6 dynamical and moisture factors (particularly WCBs)
467 appears to be linked to and mirrored by the enhanced tropospheric ridging over eastern sections.
468 This enhanced ridging is most likely related to the net cross-isentropic transport of low-PV air
469 into the tropopause region within the WCBs, resulting from the destruction of PV above the
470 diabatic heating maximum (Wernli and Davies 1997, Grams et al. 2011). Not surprisingly,
471 extreme precipitation in these patterns, versus ordinary precipitation, is more likely to feature
472 tropospheric ridging (Figs. 13a, 14a), strong southerly IVT (Fig. 13d, 14d), and WCBs (Figs.
473 13e, 14e).

4 Summary

Previously, six large-scale meteorological patterns (LSMPs) of dynamic tropopause height associated with extreme precipitation in the Northeast were identified by Agel et al. (2017). In this study, we examine the three-dimensional structure associated with these LSMPs, in terms of circulation patterns and factors relevant to precipitation, including moisture, stability, and synoptic mechanisms associated with lifting. Within each pattern, the link between the different factors and extreme precipitation is further investigated by comparing the relative strength of the factors between days with and without the occurrence of extreme precipitation. The relevant factors linked to extreme precipitation differ among the patterns, but in general include abundant moisture from integrated vapor transport (IVT) and low-level moisture convergence (LLMC) acting in the presence of synoptic-scale mechanisms for ascent, such as frontal boundaries and warm conveyor belts (WCBs) associated with extratropical storms. In Fig. 15 we summarize and outline the dominant mechanisms for extreme precipitation for each of the patterns.

The LSMPs include a ridge pattern (C1), a shallow trough/ridge pattern (C4), two seasonal variations of "eastern troughs" (C2, C5) and two seasonal variations of "Ohio Valley" troughs (C3, C6). The ridge and trough/ridge patterns are significant in that they represent nearly 45% of the extreme precipitation days, but the precipitation in these patterns is often not directly associated with nearby synoptic storms. In contrast, the other patterns are more directly linked to synoptic dynamics. For example, the eastern trough patterns feature extreme precipitation that occurs near synoptic storms nearly 90% of the time.

Extreme precipitation occurring in conjunction with a widespread tropopause ridge in the Northeast (C1) appears to be generated by a number of processes. Precipitation under these

497 ridges is generally light at the grid level, suggesting localized extremes. Although these
498 extremes can occur at any station, they more commonly occur inland along the New
499 York/Canadian border. Consistent factors associated with these extremes include anomalous
500 moisture feed (IVT) from the Great Lakes, sometimes remaining in place for several days
501 leading up to the extreme event, and enhanced LLMC. Potential for convective activity is
502 strongest in this pattern. Weak Great Lakes synoptic storms (perhaps related to shortwaves
503 embedded in the upper-level flow), along with their attendant cold and warm fronts, are also
504 associated with inland extremes. In addition, some cold fronts may be associated with low-level
505 thermal contrasts due to organized convection, or be extensions of cold fronts draped across the
506 Northeast and originating from synoptic systems located well to the north of the region.
507 For the other patterns (the shallow trough/ridge, the eastern troughs, and the Ohio Valley
508 troughs), the presence of nearby synoptic storms is critical to understanding the processes that
509 lead to extreme precipitation. The warm-season trough/ridge pattern C4 appears to be related
510 inland to ample moisture flow and moderate synoptic forcing associated with enhanced
511 instability and a storm track to the west of the region. For the eastern troughs C2 and C5,
512 dynamical lift is generated by quasi-geostrophic (QG) forcing, which is particularly strong for
513 the wintertime C2 pattern. The C2 pattern appears to represent classic 'nor'easter-type' synoptic
514 storms, with strong southerly flow of moisture up to 48 hours before extreme events in the
515 presence of WCBs just offshore; while the C5 pattern represents a warm-season shallow trough
516 in nearly the same location, but with comparatively less moisture availability, and the strongest
517 dynamical forcing mechanisms to the west in the form of cold fronts, and in Maine with warm
518 fronts related to offshore WCBs. In contrast, the wintertime Ohio Valley troughs C3 and C6
519 represent storms travelling inland from the Atlantic seaboard through New England. Abundant

520 moisture transported from the south ahead of the storms, and vigorous upward motion associated
521 with the accompanying WCBs account for many of the precipitation extremes in these patterns,
522 with QG forcing linked to some extremes in western New York.
523 All patterns show stronger IVT on extreme precipitation days, with southerly anomalies
524 for the eastern and Ohio Valley troughs, southwesterly anomalies for the trough/ridge C4 and
525 near-westerly anomalies for ridge pattern C1. The IVT differences are among the largest
526 magnitude differences between extreme and non-extreme days and indicate that moisture
527 availability is a very important ingredient for extreme precipitation production in each pattern
528 type. In addition, moisture transport tends to be more southerly on extreme days than for non-
529 extreme days for each pattern type. By constructing a simple "IVT index" of standardized
530 anomalies of mean IVT over a select area (38°N–48°N, 82°W–67°W), we find that 23.9% of
531 extreme IVT days (defined here as 2.5+ standard anomalies) occur in conjunction with extreme
532 precipitation, while 9.9% of extreme precipitation days involve extreme IVT. For pattern C6, this
533 number is larger, with 27.5% of the extreme days featuring extreme IVT.
534 Equally important for generating extreme precipitation as opposed to ordinary
535 precipitation within the trough patterns is the presence of WCBs. In fact, the differences of WCB
536 frequency between extreme and non-extreme precipitation days for each of the patterns,
537 including the ridge C1 and the shallow trough/ridge C4, are among the largest standardized
538 differences for the patterns. To better quantify the relationship between extreme precipitation and
539 WCBs for the Northeast, we calculate the mean WCB frequency over the domain for each day
540 containing at least one WCB, and define the top 10% as "high WCB frequency days". We find
541 that for Ohio Valley trough C6, 43.5% of extreme precipitation occurs on high WCB frequency
542 days. For C2 and C3, the values drop to 25.6% and 20.6%, respectively, but are still considerably

543 higher than that for the ridge patterns C1 (5%) and C4 (5.4%), and the summertime eastern
544 trough C5 (2.5%). Tools such as the "IVT index" or "high WCB frequency days" can be
545 valuable additions to the compositing techniques largely used here to identify the factors
546 associated with extreme precipitation.

547 In this study we look at several upper-level patterns, or LSMPs, that occur during
548 extreme precipitation events, and seek to understand how the key processes and ingredients for
549 extreme precipitation (i.e. lift mechanisms, moisture, and instability) are informed by those
550 patterns. Our approach focuses on composite representations of these factors. To the extent that
551 individual pattern days share the same features as the composites, this provides a reasonable
552 first-order assessment of what leads to extreme precipitation for various upper-level circulation
553 patterns. However, individual events within each pattern type may yield quite different results.
554 For example, for the summertime eastern trough C5, manual inspection reveals that some days
555 feature large levels of instability, while others feature greater lift due to synoptic QG forcing. An
556 important next step is to investigate representative days within these pattern types for a more
557 nuanced understanding of how extreme precipitation is generated, and to determine if the LSMPs
558 can be further broken into representative sub-patterns. In addition, it is important to understand
559 how these large-scale factors interact with sub-grid-scale processes. To this end, we intend to
560 look more closely at the frontal processes (QG, slantwise instability, and other mesoscale
561 dynamics) implicated in extreme precipitation, which are best done by event, or within an event-
562 centric framework. As a final step, we also intend to examine the explanatory power of the
563 extreme precipitation factors identified here, perhaps through the use of simple predictive models
564 and measures such as the "IVT index".
565

566 **Table 1** Relative frequency (%) of select categories within each pattern type C1–C6. Categories
567 are based on station location (coastal or inland) and nearness (within 800 km) to Era-Interim
568 storm tracks on day of extreme precipitation. Frequencies higher (lower) than expected due to
569 chance are followed by an "H" ("L"), based on Monte Carlo resampling
570

Category	**C1**	**C2**	**C3**	**C4**	**C5**	**C6**
Coastal	27.1(L)	63.7(H)	43.2	33.3(L)	40.0	40.9
Inland	72.9(H)	36.3(L)	56.8	66.7(H)	60.0	59.1
Storm-related	70.3(L)	90.7(H)	76.8	77.9	88.7(H)	80.3
Non-Storm-related	29.7(H)	09.3(L)	23.2	22.1	11.3(L)	19.7
Coastal/Storm	22.7(L)	59.1(H)	29.2	25.5(L)	38.0	31.4
Coastal/Non-Storm	04.4	04.7	14.0(H)	07.9	02.1(L)	09.5
Inland/Storm	47.6	31.7(L)	47.6	52.4(H)	50.8	48.9
Inland/Non-Storm	25.3(H)	04.6(L)	09.2	14.2	9.23	10.2

571

572 **References**

573 Agel L, Barlow M, Feldstein SB, Gutowski WJ (2017) Identification of large-scale
574 meteorological patterns associated with extreme precipitation in the US northeast.
575 Climate Dynamics doi:10.1007/s00382-017-3724-8

576 Agel L, Barlow M, Qian J-H, Colby F, Douglas E, Eichler T (2015) Climatology of Daily
577 Precipitation and Extreme Precipitation Events in the Northeast United States. Journal of
578 Hydrometeorology 16:2537-2557 doi:doi:10.1175/JHM-D-14-0147.1

579 Berry G, Jakob C, Reeder M (2011) Recent global trends in atmospheric fronts. Geophysical
580 Research Letters 38:n/a-n/a doi:10.1029/2011GL049481

581 Binder H, Boettcher M, Joos H, Wernli H (2016) The role of warm conveyor belts for the
582 intensification of extratropical cyclones in Northern Hemisphere winter. Journal of the
583 Atmospheric Sciences 73:3997-4020 doi:10.1175/jas-d-15-0302.1

584 Browning KA (1990) Organization of clouds and precipitation in extratropical cyclones.
585 Extratropical Cyclones: The Erik Palmén Memorial Volume, C. W. Newton, and E. O.
586 Holopainen, Eds., Amer. Meteor. Soc., 129–153.

587 Catto JL, Jakob C, Berry G, Nicholls N (2012) Relating global precipitation to atmospheric
588 fronts. Geophysical Research Letters 39:n/a-n/a doi:10.1029/2012GL051736

589 Catto JL, Madonna E, Joos H, Rudeva I, Simmonds I (2015) Global Relationship between Fronts
590 and Warm Conveyor Belts and the Impact on Extreme Precipitation Journal of Climate
591 28:8411-8429 doi:10.1175/jcli-d-15-0171.1

592 Catto JL, Nicholls N, Jakob C, Shelton KL (2014) Atmospheric fronts in current and future
593 climates Geophysical Research Letters 41:7642-7650 doi:10.1002/2014GL061943

594 Catto JL, Pfahl S (2013) The importance of fronts for extreme precipitation. Journal of

595 Geophysical Research: Atmospheres 118:10,791-710,801 doi:10.1002/jgrd.50852
596 Catto JL, Shaffrey LC, Hodges KI (2010) Can Climate Models Capture the Structure of
597 Extratropical Cyclones? Journal of Climate 23:1621-1635 doi:10.1175/2009jcli3318.1
598 Chen M, Xie P, and Co-authors (2008) CPC Unified Gauge-based Analysis of Global Daily
599 Precipitation
600 Collow ABM, Bosilovich MG, Koster RD (2016) Large-Scale Influences on Summertime Extreme
601 Precipitation in the Northeastern United States. Journal of Hydrometeorology 17:3045-3061
602 doi:10.1175/jhm-d-16-0091.1
603 Dee DP et al. (2011) The ERA-Interim reanalysis: configuration and performance of the data
604 assimilation system. Quarterly Journal of the Royal Meteorological Society 137:553-597
605 doi:10.1002/qj.828
606 Diday E, Simon JC (1976) Clustering Analysis. In: Fu KS (ed) Digital Pattern Recognition.
607 Springer Berlin Heidelberg, Berlin, Heidelberg, pp 47-94. doi:10.1007/978-3-642-96303-
608 2_3
609 Dowdy AJ, Catto JL (2017) Extreme weather caused by concurrent cyclone, front and
610 thunderstorm occurrences 7:40359 doi:10.1038/srep40359
611 https://www.nature.com/articles/srep40359#supplementary-information
612 Easterling DR, Karl TR, Lawrimore JH, Del Greco SA (1999) United States Historical
613 Climatology Network daily temperature, precipitation, and snow data for 1871-1997.
614 Glisan JM, Gutowski WJ (2014) WRF winter extreme daily precipitation over the North
615 American CORDEX Arctic Journal of Geophysical Research: Atmospheres 119:10,738-
616 710,748 doi:10.1002/2014JD021676
617 Grams CM et al. (2011) The key role of diabatic processes in modifying the upper-tropospheric

618 wave guide: a North Atlantic case-study. Quarterly Journal of the Royal Meteorological
619 Society 137:2174-2193 doi:10.1002/qj.891
620 Green JSA, Ludlam HF, McIlveen JFR (1966) Isentropic relative-flow analysis and the parcel
621 theory vol 92. doi:10.1002/qj.49709239204
622 Groisman PY, Knight RW, Zolina OG (2013) Recent trends in regional and global extreme
623 precipitation patterns. In: Sr. RP, Hossain F (eds) Climate Vulnerability: Understanding
624 and Addressing Threats to Essential Resources. Volume 5, Vulerability of Water
625 Resources to Climate. Elsevier Publishing House, pp 25-55
626 Grotjahn R et al. (2016) North American extreme temperature events and related large scale
627 meteorological patterns: a review of statistical methods, dynamics, modeling, and trends.
628 Climate Dynamics 46:1151-1184 doi:10.1007/s00382-015-2638-6
629 Harrold TW (1973) Mechanisms influencing the distribution of precipitation within baroclinic
630 disturbances. Quarterly Journal of the Royal Meteorological Society 99:232-251
631 doi:10.1002/qj.49709942003
632 Hewson TD (1998) Objective fronts. Meteorological Applications 5:37-65
633 doi:10.1017/S1350482798000553
634 Holton JR (2004) An Introduction to dynamic Meteorology - Fourth Edition. Elsevier Academic
635 Press, Massachusetts, USA
636 Hoskins BJ, Hodges KI (2002) New Perspectives on the Northern Hemisphere Winter Storm
637 Tracks. Journal of the Atmospheric Sciences 59:1041-1061 doi:10.1175/1520-
638 0469(2002)059<1041:npotnh>2.0.co;2
639 Hoskins BJ, McIntyre ME, Robertson AW (1985) On the use and significance of isentropic
640 potential vorticity maps Quarterly Journal of the Royal Meteorological Society 111:877-

946 doi:10.1002/qj.49711147002

Kocin PJ, Uccellini LW (2004) Volume I: Overview Meteorological Monographs 32:1-289 doi:10.1175/0065-9401-32.54.1; M3: doi: 10.1175/0065-9401-32.54.1; 04 10.1175/0065-9401-32.54.1

Kohonen T (2001) Self-Organizing Maps. Springer-Verlag New York, Inc.

Kunkel KE, Easterling DR, Kristovich DAR, Gleason B, Stoecker L, Smith R (2012) Meteorological Causes of the Secular Variations in Observed Extreme Precipitation Events for the Conterminous United States. Journal of Hydrometeorology 13:1131-1141 doi:10.1175/jhm-d-11-0108.1

Kunkel K, Coauthors (2013) Regional Climate Trends and Scenarios for the U.S. National Climate Assessment. Part 1. Climate of the Northeast U.S. NOAA Technical Report NESDIS 142-1, 80 pp.

Landsea CW, Franklin JL (2013) Atlantic Hurricane Database Uncertainty and Presentation of a New Database Format. Monthly Weather Review 141:3576-3592 doi:10.1175/MWR-D-12-00254.1

Loikith PC, Broccoli AJ (2012) Characteristics of Observed Atmospheric Circulation Patterns Associated with Temperature Extremes over North America Journal of Climate 25:7266-7281 doi:10.1175/jcli-d-11-00709.1

Madonna E, Wernli H, Joos H, Martius O (2014) Warm Conveyor Belts in the ERA-Interim Dataset (1979–2010). Part I: Climatology and Potential Vorticity Evolution. Journal of Climate 27:3-26 doi:doi:10.1175/JCLI-D-12-00720.1

Maglaras GJ, Waldstreicher JS, Kocin PJ, Gigi AF, Marine RA (1995) Winter Weather Forecasting throughout the Eastern United States. Part I: An Overview. Weather and

664 Forecasting 10:5-20 doi:10.1175/1520-0434(1995)010<0005:WWFTTE>2.0.CO;2
665 Melillo JM, Richmond TC, Yohe GW (2014) Climate Change Impacts in the United States: The
666 Third National Climate Assessment. doi:10.7930/J0Z31WJ2
667 Michelangeli P-A, Vautard R, Legras B (1995) Weather Regimes: Recurrence and Quasi
668 Stationarity. Journal of the Atmospheric Sciences 52:1237-1256 doi:doi:10.1175/1520-
669 0469(1995)052<1237:WRRAQS>2.0.CO;2
670 Milrad SM, Atallah EH, Gyakum JR, Dookhie G (2014) Synoptic Typing and Precursors of
671 Heavy Warm-Season Precipitation Events at Montreal, Québec. Weather and Forecasting
672 29:419-444 doi:doi:10.1175/WAF-D-13-00030.1
673 Muller CJ, O'Gorman PA, Back LE (2011) Intensification of Precipitation Extremes with
674 Warming in a Cloud-Resolving Model. Journal of Climate 24:2784-2800
675 Nielsen-Gammon JW (2001) A Visualization of the Global Dynamic Tropopause Bulletin of the
676 American Meteorological Society 82:1151-1167 doi:doi:10.1175/1520-
677 0477(2001)082<1151:AVOTGD>2.3.CO;2
678 Pfahl S, Madonna E, Boettcher M, Joos H, Wernli H (2014) Warm Conveyor Belts in the ERA-
679 Interim Dataset (1979-2010). Part II: Moisture Origin and Relevance for Precipitation.
680 Journal of Climate 27:27-40 doi:10.1175/JCLI-D-13-00223.1
681 Pfahl S, Sprenger M (2016) On the relationship between extratropical cyclone precipitation and
682 intensity. Geophysical Research Letters 43:1752-1758 doi:10.1002/2016GL068018
683 Pfahl S, Wernli H (2012) Quantifying the Relevance of Cyclones for Precipitation Extremes.
684 Journal of Climate 25:6770-6780 doi:10.1175/jcli-d-11-00705.1
685 Pomroy HR, Thorpe AJ (2000) The Evolution and Dynamical Role of Reduced Upper-
686 Tropospheric Potential Vorticity in Intensive Observing Period One of FASTEX.

687 Monthly Weather Review 128:1817-1834 doi:10.1175/1520-
688 0493(2000)128<1817:teadro>2.0.co;2
689 Rienecker MM et al. (2011) MERRA: NASA's Modern-Era Retrospective Analysis for Research
690 and Applications. Journal of Climate 24:3624-3648 doi:10.1175/jcli-d-11-00015.1
691 Roller CD, Qian J-H, Agel L, Barlow M, Moron V (2016) Winter Weather Regimes in the
692 Northeast United States. Journal of Climate 29:2963-2980 doi:10.1175/JCLI-D-15-
693 0274.1
694 Saha S et al. (2014) The NCEP Climate Forecast System Version 2 Journal of Climate 27:2185-
695 2208 doi:10.1175/jcli-d-12-00823.1
696 Schumacher RS, Johnson RH (2005) Organization and Environmental Properties of Extreme-
697 Rain-Producing Mesoscale Convective Systems. Monthly Weather Review 133:961-976
698 doi:doi:10.1175/MWR2899.1
699 Sprenger M, Wernli H (2015) The LAGRANTO Lagrangian analysis tool – version 2.0 vol 8.
700 doi:10.5194/gmd-8-2569-2015
701 Stoelinga MT (1996) A Potential Vorticity-Based Study of the Role of Diabatic Heating and
702 Friction in a Numerically Simulated Baroclinic Cyclone. Monthly Weather Review
703 124:849-874 doi:10.1175/1520-0493(1996)124<0849:apvbso>2.0.co;2
704 Wernli H, Davies HC (1997) A lagrangian-based analysis of extratropical cyclones. I: The
705 method and some applications. Quarterly Journal of the Royal Meteorological Society
706 123:467-489 doi:10.1002/qj.49712353811
707 Wernli H (1997) A Lagrangian-based analysis of extratropical cyclones. II: A detailed case-study.
708 Quarterly Journal of the Royal Meteorological Society 123:1677–1706
709 doi:10.1002/qj.49712354211

710

711 **Figure Captions**

712

713 **Fig. 1** Results of k-means separation of MERRA blended tropopause height anomalies for 691
714 top 1% extreme precipitation days, 1979-2008, into six patterns C1–C6, showing (a) composites
715 of tropopause pressure (contours, in 20 hPa intervals, and anomalies, shaded), (b) seasonal
716 frequency (expressed as a percent) of each pattern (red if greater than that expected due to
717 chance, blue if less than that expected due to chance, black otherwise), and (c) the percentage of
718 pattern days accounted for by extremes at each station (black dots, with size proportional to
719 percentage, ranging from 0 to 8 percent), overlaid on CPCU gridded precipitation anomaly
720 composite for each pattern (shaded, mm) . The text above each pattern in (a) indicates the
721 number of dates in each composite. The significance in (b) is based on 95% confidence interval
722 using Monte Carlo sampling (shown as grey boxes). Anomalies calculated by subtracting 30-
723 year smoothed daily mean from daily values. Figure reproduced from Agel et al. (2017)

724

725 **Fig. 2** Composite fields for ridge pattern C1 days, showing a) 200-hPa wind magnitude (m s^{-1},
726 contours and shaded anomalies) and direction (arrows), b) 500-hPa geopotential height (dm,
727 contours and shaded anomalies), c) MSLP (hPa, contours and shaded anomalies), d) 700-hPa
728 vertical velocity anomalies (Pa s^{-1}, shaded), e) LLMC, represented by lowest model-level wind
729 anomalies (m s^{-1}, arrows) and lowest model-level specific humidity anomalies (g kg^{-1}, shaded), f)
730 IVT magnitude (kg m^{-1} s^{-1}, contours and shaded anomalies) and direction (arrows), g) 750-hPa
731 static stability (K Pa^{-1}, contours and shaded anomalies), h) CFSR CAPE (J kg^{-1}, shaded
732 anomalies) at 18 UTC, i) QG forcing based on thermal wind formulation, i.e. 700-hPa relative
733 vorticity ($1e^{-5}$ s^{-1}, shaded) advection by the 900–500 hPa thermal wind (isotherms of 900–500

734 thickness, m, are shown to indicate thermal wind direction), j) WCB trajectory frequency, i.e.
735 percentage of extreme precipitation days associated with at least one WCB at each grid point
736 (below 500 hPa, color shading, and above 500 hPa, blue contours for 5, 10, 20, 30, 40 and 50%),
737 potential vorticity at 315K (thick black contours for 2, 3 and 4 PVU), and MSLP (black contours
738 every 3 hPa), k) Ertel's PV anomaly cross-sections (shaded, PVU) at 43°N for 900-200 hPa, and
739 l) density of warm fronts (red shading) and cold fronts (red shading) relative to stations
740 experiencing extreme precipitation (black dot in center of 40° longitude x 36° latitude grid),
741 separated into storm-related (within 800 km of Era-Interim storm track based on 850-hPa relative
742 vorticity) and non-storm-related extremes. Unless otherwise noted, all fields are from MERRA
743 and evaluated at 12 UTC
744
745 **Fig. 3** 500-hPa geopotential height (dm) and relative vorticity ($1e^{-5}$ s^{-1}, shaded), relative to
746 stations experiencing extreme precipitation (black dot in center of 40° longitude x 36° latitude
747 grid) for (a) storm-related extreme precipitation, and (b) non-storm-related extreme precipitation
748 for ridge pattern C1.
749
750 **Fig. 4** Extreme day composite minus non-extreme day composite for SOM4 (similar to C1),
751 showing differences in standardized a) tropopause height anomalies, b) MSLP anomalies, c)
752 LLMC anomalies, d) IVT anomalies, e) WCB frequencies, and f) CAPE anomalies. The fields
753 are standardized before differencing by dividing by the temporal standard deviation. Only
754 differences significant to the 0.05 level are shown
755
756 **Fig. 5** Same as Fig. 2, but for trough/ridge pattern C4

757

758 **Fig. 6** Same as Fig. 4, but for SOM8 (similar to C4)

759

760 **Fig. 7** Same as Fig. 2, but for eastern trough C2

761

762 **Fig. 8** Same as Fig. 2, but for eastern trough C5

763

764 **Fig. 9** Same as Fig. 4, but for SOM26 (similar to C2), and with f) thermal wind form of QG

765 forcing, i.e. 700-hPa relative vorticity and 900–500 hPa thermal wind (arrows)

766

767 **Fig. 10** Same as Fig. 9, but for SOM20 (similar to C5)

768

769 **Fig. 11** Same as Fig. 2, but for Ohio Valley trough C3

770

771 **Fig. 12** Same as Fig. 2, but for Ohio Valley trough C6

772

773 **Fig. 13** Same as Fig. 9, but SOM13 (similar to C3)

774

775 **Fig. 14** Same as Fig. 9, but for SOM1 (similar to C6)

776

777 **Fig. 15** Identification of key ingredients and processes linked to extreme precipitation for each of

778 the k-means patterns C1–C6. Shown are dominant moisture processes (LLMC, IVT, WCBs;

779 green arrows), cold fronts, warm fronts, and low pressure centers (orange L symbol), and station

780 locations experiencing extremes (black dots, with size of dot indicating relative frequency of
781 extremes within pattern)
782

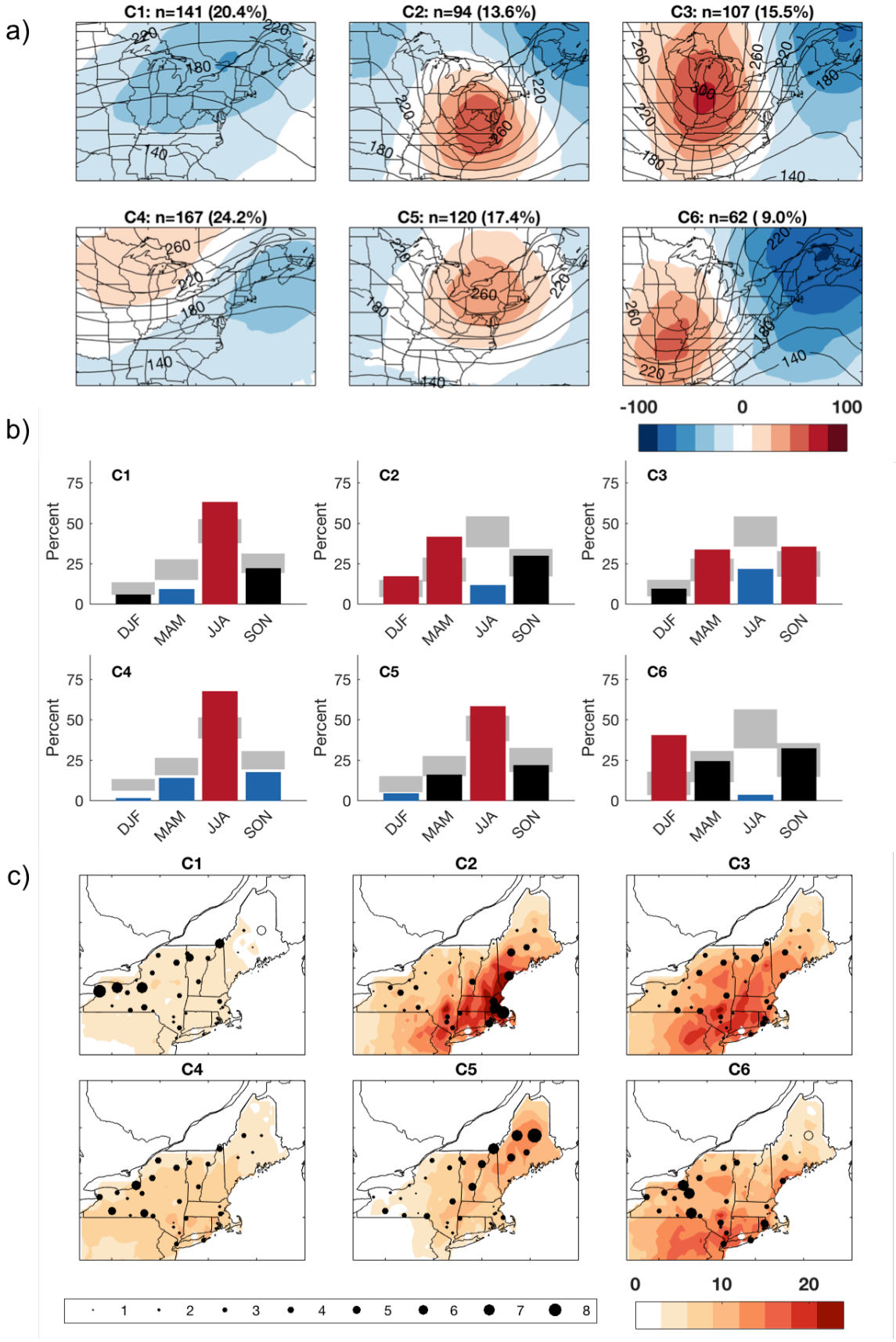
a)
C1: n=141 (20.4%)
C2: n=94 (13.6%)
C3: n=107 (15.5%)
C4: n=167 (24.2%)
C5: n=120 (17.4%)
C6: n=62 (9.0%)
-100
0
100
b)
C1
C2
C3
C4
C5
C6
Percent
DJF
MAM
JJA
SON
c)
0
10
20

Fig. 1 Results of k-means separation of MERRA blended tropopause height anomalies for 691 top 1% extreme precipitation days, 1979-2008, into six patterns C1–C6, showing (a) composites of tropopause pressure (contours, in 20 hPa intervals, and anomalies, shaded), (b) seasonal frequency (expressed as a percent) of each pattern (red if greater than that expected due to chance, blue if less than that expected due to chance, black otherwise), and (c) the percentage of pattern days accounted for by extremes at each station (black dots, with size proportional to percentage, ranging from 0 to 8 percent), overlaid on CPCU gridded precipitation anomaly composite for each pattern (shaded, mm) . The text above each pattern in (a) indicates the number of dates in each composite. The significance in (b) is based on 95% confidence interval using Monte Carlo sampling (shown as grey boxes). Anomalies calculated by subtracting 30-year smoothed daily mean from daily values. Figure reproduced from Agel et al. (2017)

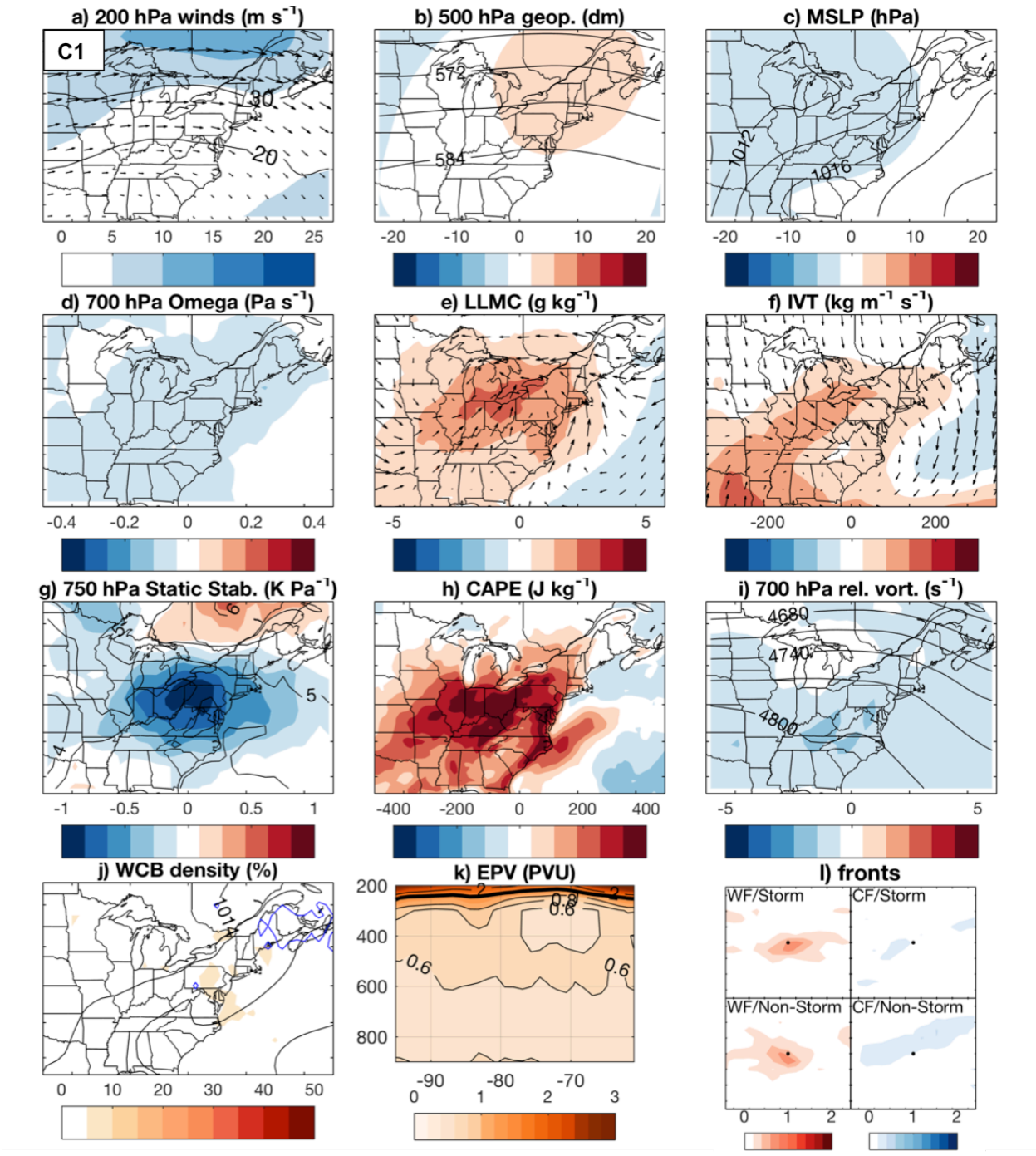

Fig. 2 Composite fields for ridge pattern C1 days, showing a) 200-hPa wind magnitude (m s^{-1}, contours and shaded anomalies) and direction (arrows), b) 500-hPa geopotential height (dm, contours and shaded anomalies), c) MSLP (hPa, contours and shaded anomalies), d) 700-hPa vertical velocity anomalies (Pa s^{-1}, shaded), e) LLMC, represented by lowest model-level wind

anomalies (m s^{-1}, arrows) and lowest model-level specific humidity anomalies (g kg^{-1}, shaded), f) IVT magnitude (kg m^{-1} s^{-1}, contours and shaded anomalies) and direction (arrows), g) 750-hPa static stability (K Pa^{-1}, contours and shaded anomalies), h) CFSR CAPE (J kg^{-1}, shaded anomalies) at 18 UTC, i) QG forcing based on thermal wind formulation, i.e. 700-hPa relative vorticity ($1e^{-5}$ s^{-1}, shaded) advection by the 900–500 hPa thermal wind (isotherms of 900–500 thickness, m, are shown to indicate thermal wind direction), j) WCB trajectory frequency, i.e. percentage of extreme precipitation days associated with at least one WCB at each grid point (below 500 hPa, color shading, and above 500 hPa, blue contours for 5, 10, 20, 30, 40 and 50%), potential vorticity at 315K (thick black contours for 2, 3 and 4 PVU), and MSLP (black contours every 3 hPa), k) Ertel's PV anomaly cross-sections (shaded, PVU) at 43°N for 900-200 hPa, and l) density of warm fronts (red shading) and cold fronts (red shading) relative to stations experiencing extreme precipitation (black dot in center of 40° longitude x 36° latitude grid), separated into storm-related (within 800 km of Era-Interim storm track based on 850-hPa relative vorticity) and non-storm-related extremes. Unless otherwise noted, all fields are from MERRA and evaluated at 12 UTC

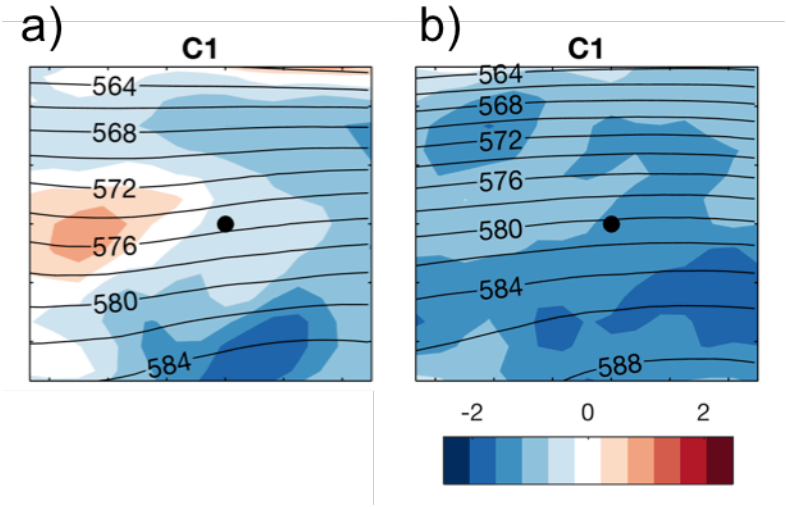

Fig. 3 500-hPa geopotential height (dm) and relative vorticity ($1e^{-5}$ s^{-1}, shaded), relative to stations experiencing extreme precipitation (black dot in center of 40° longitude x 36° latitude grid) for (a) storm-related extreme precipitation, and (b) non-storm-related extreme precipitation for ridge pattern C1.

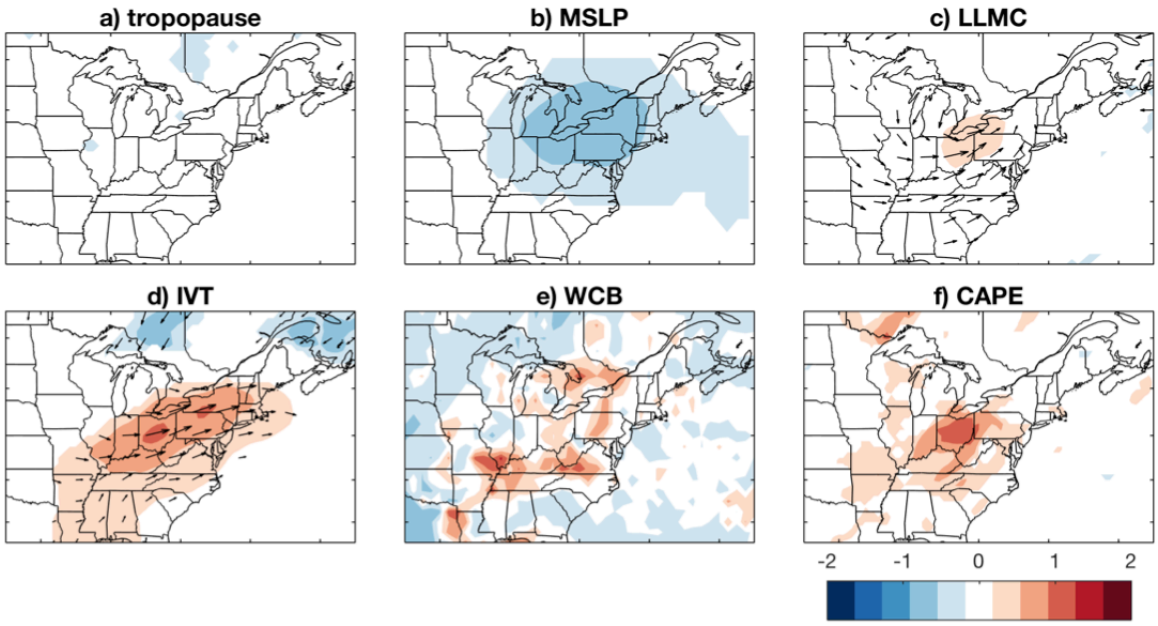

Fig. 4 Extreme day composite minus non-extreme day composite for SOM4 (similar to C1), showing differences in standardized a) tropopause height anomalies, b) MSLP anomalies, c) LLMC anomalies, d) IVT anomalies, e) WCB frequencies, and f) CAPE anomalies. The fields are standardized before differencing by dividing by the temporal standard deviation. Only differences significant to the 0.05 level are shown

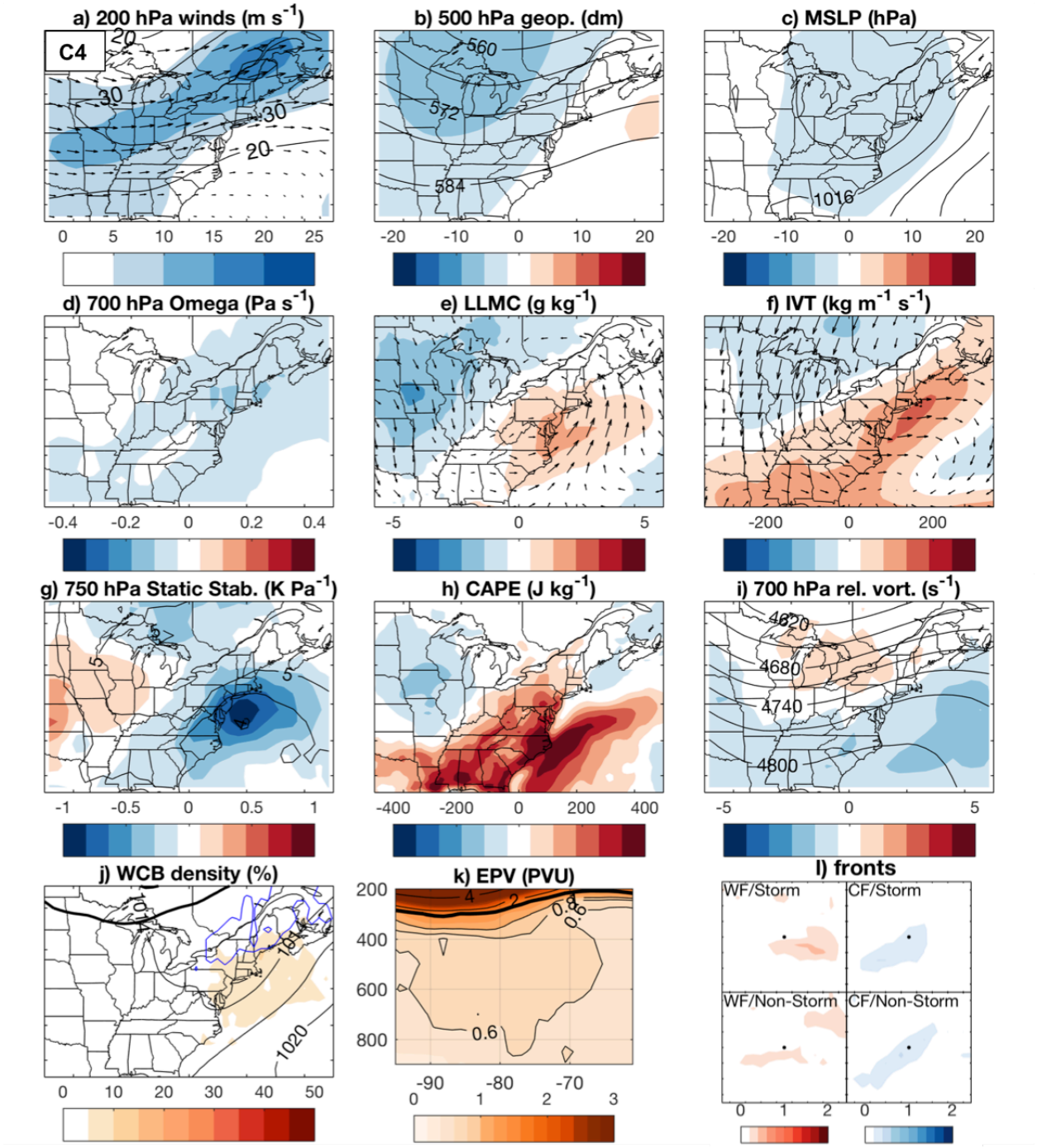

Fig. 5 Same as Fig. 2, but for trough/ridge pattern C4

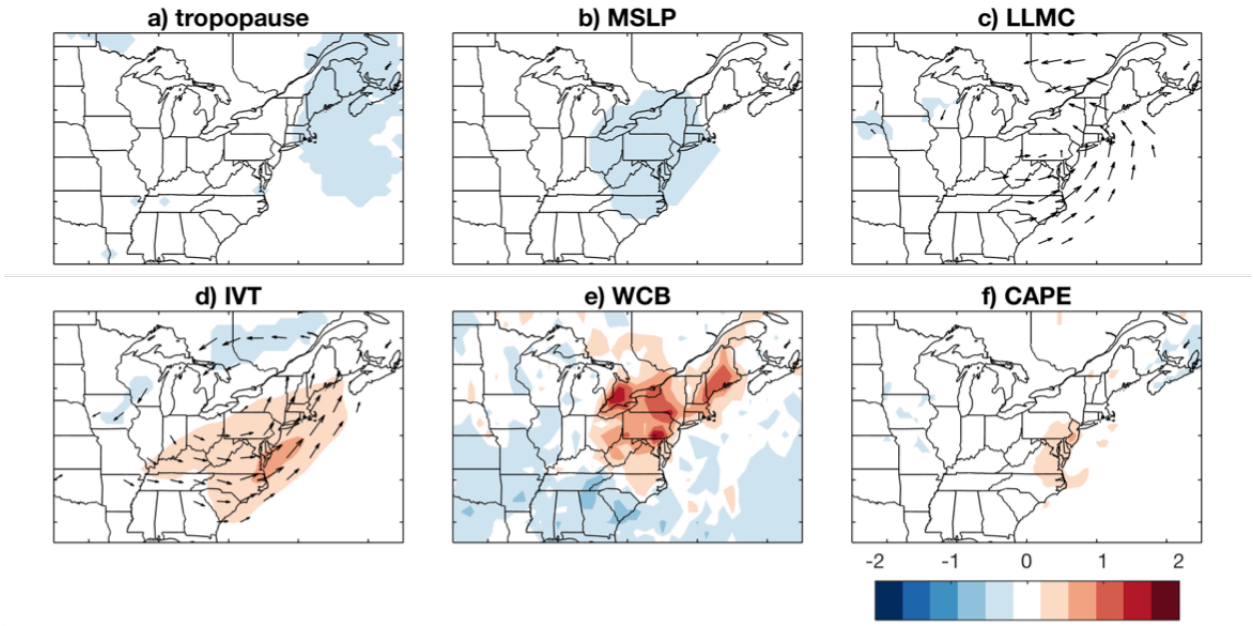

Fig. 6 Same as Fig. 3, but for SOM8 (similar to C4)

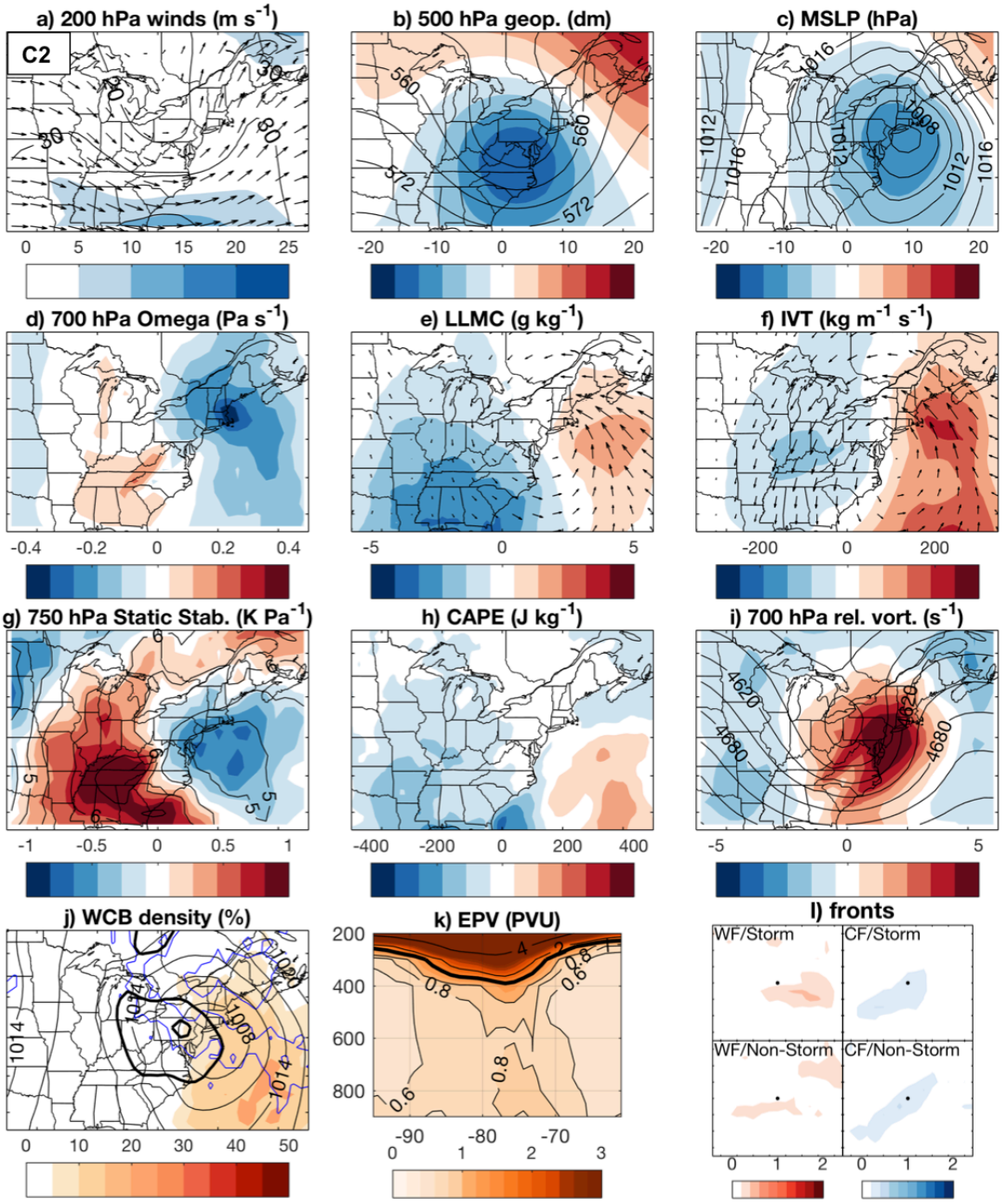

Fig. 7 Same as Fig. 2, but for eastern trough C2

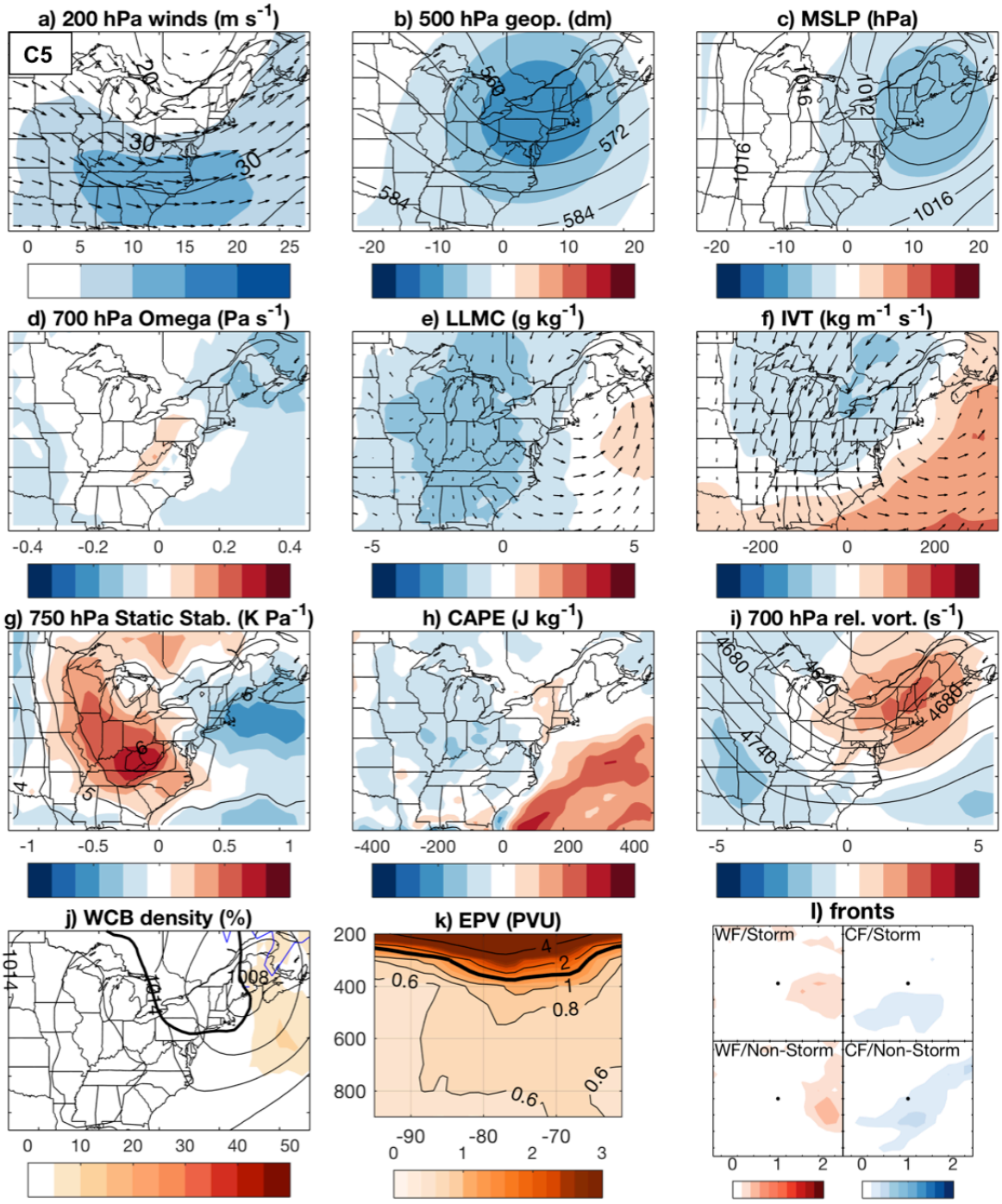

Fig. 8 Same as Fig. 2, but for eastern trough C5

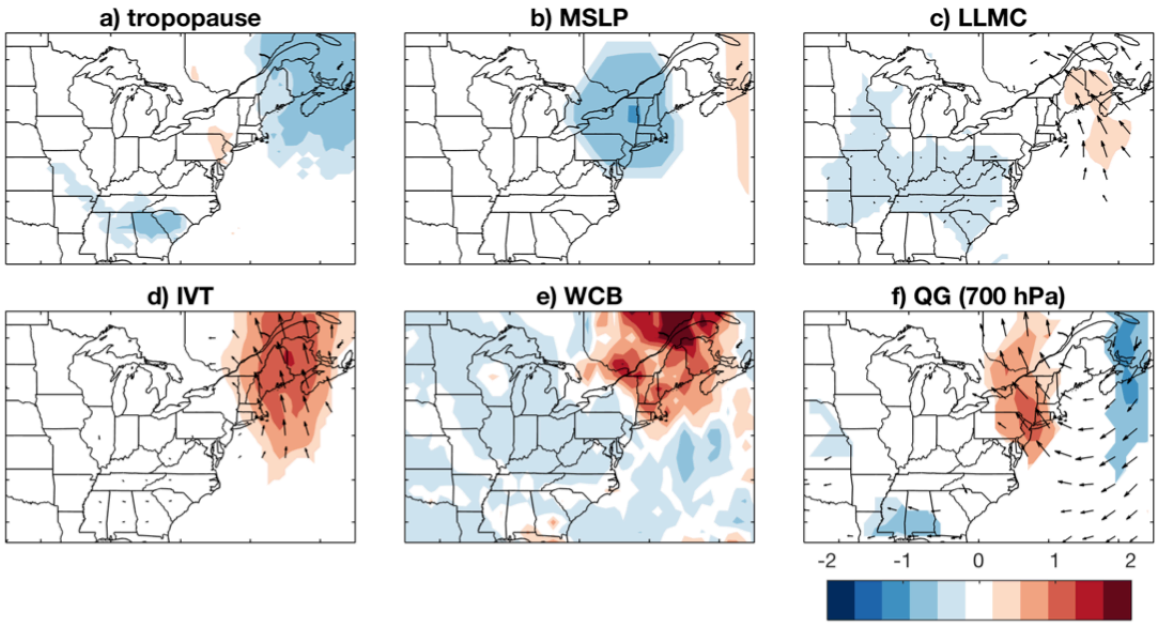

Fig. 9 Same as Fig. 3, but for SOM26 (similar to C2), and with f) thermal wind form of QG forcing, i.e. 700-hPa relative vorticity and 900–500 hPa thermal wind (arrows)

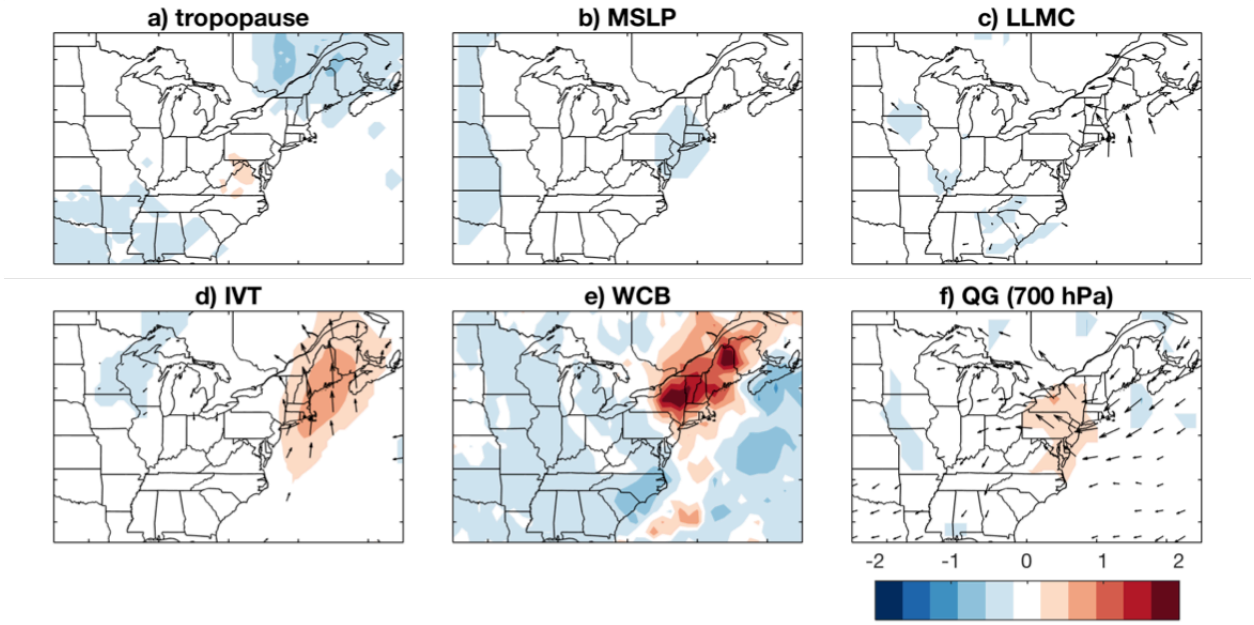

Fig. 10 Same as Fig. 9, but for SOM20 (similar to C5)

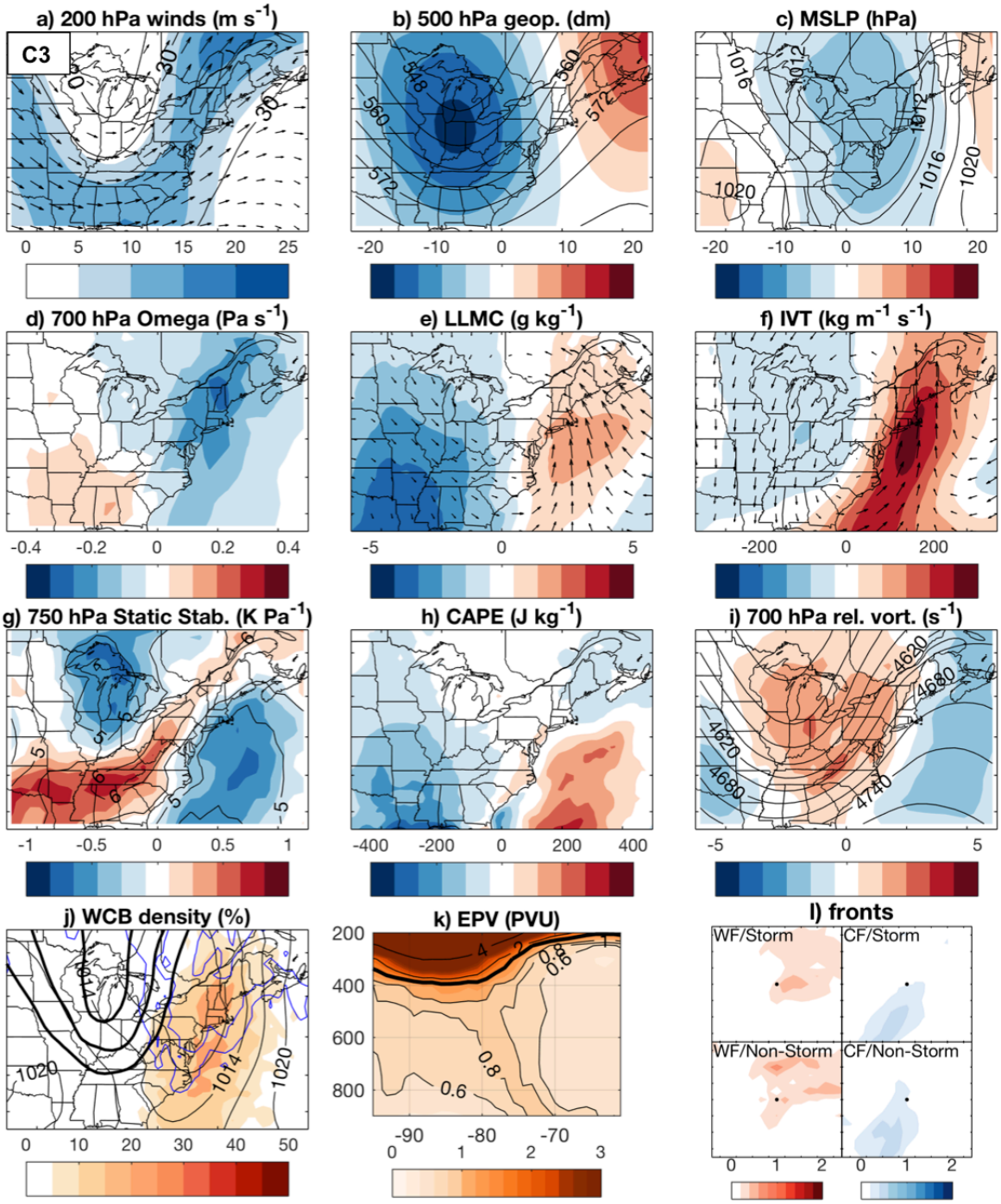

Fig. 11 Same as Fig. 2, but for Ohio Valley trough C3

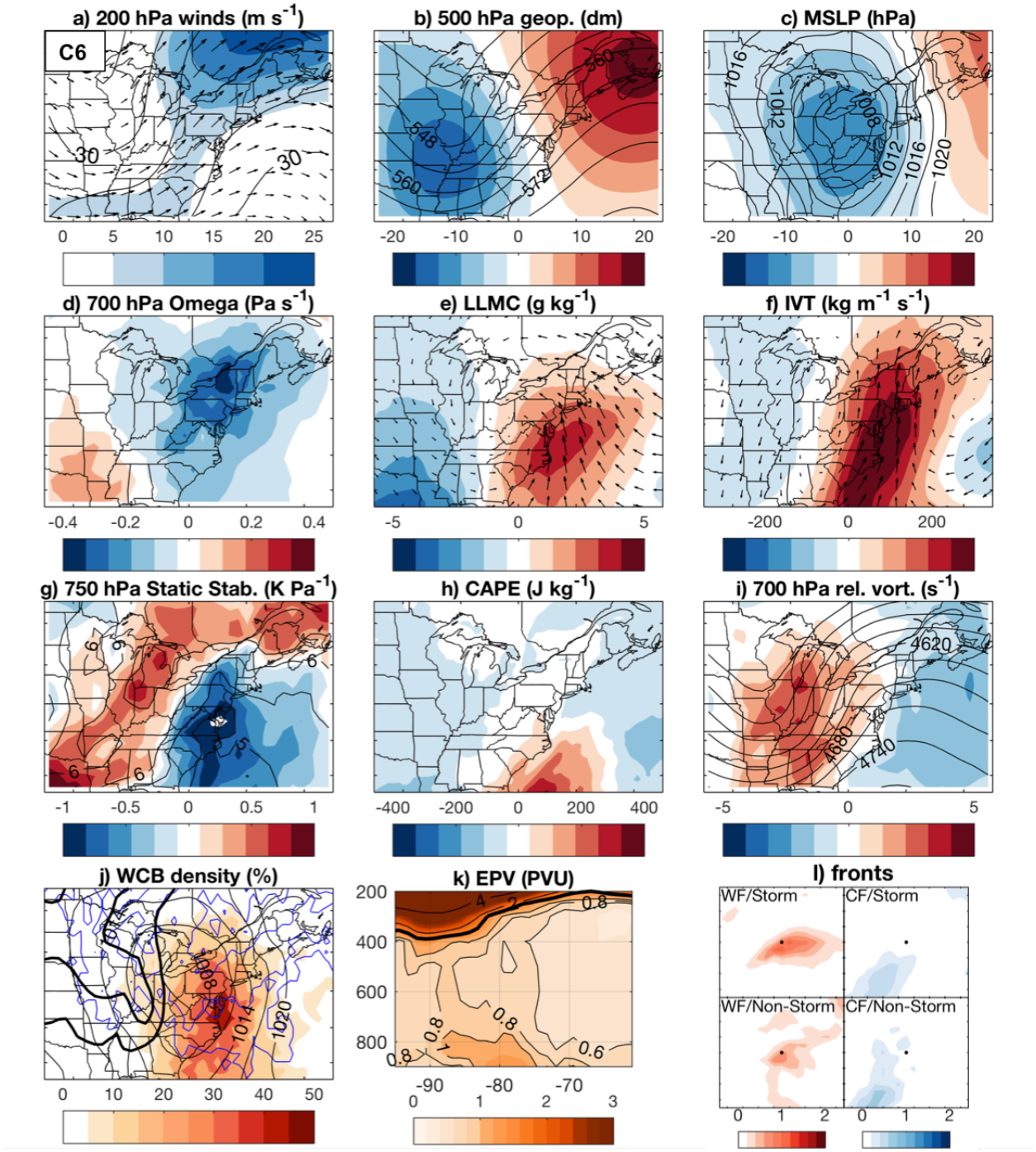

Fig. 12 Same as Fig. 2, but for Ohio Valley trough C6

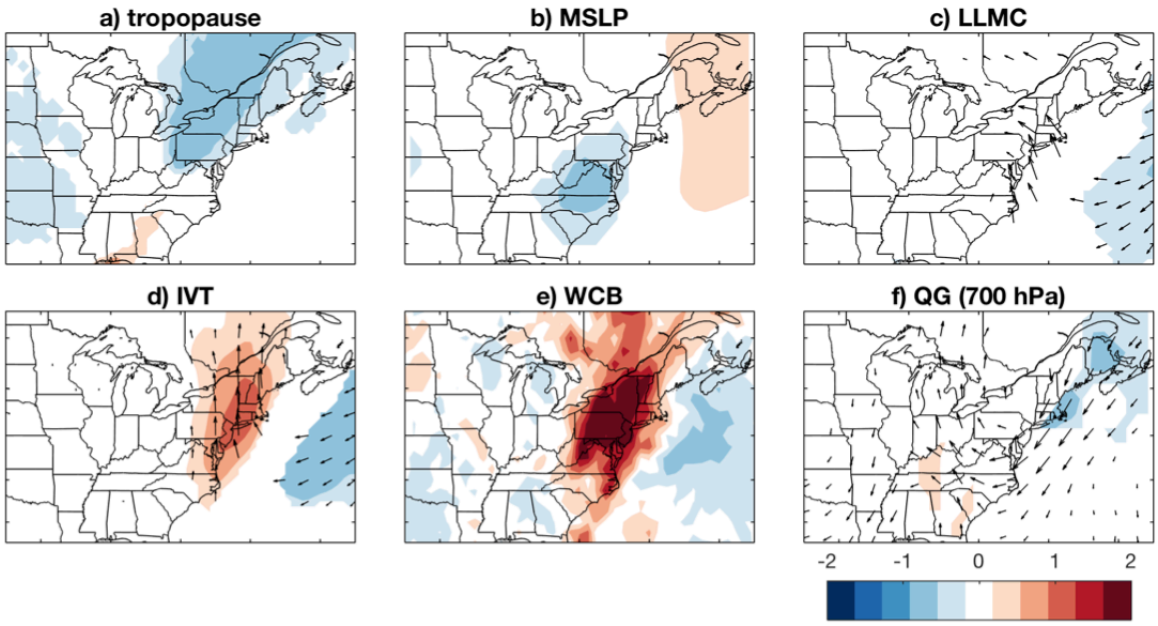

Fig. 13 Same as Fig. 9, but SOM13 (similar to C3)

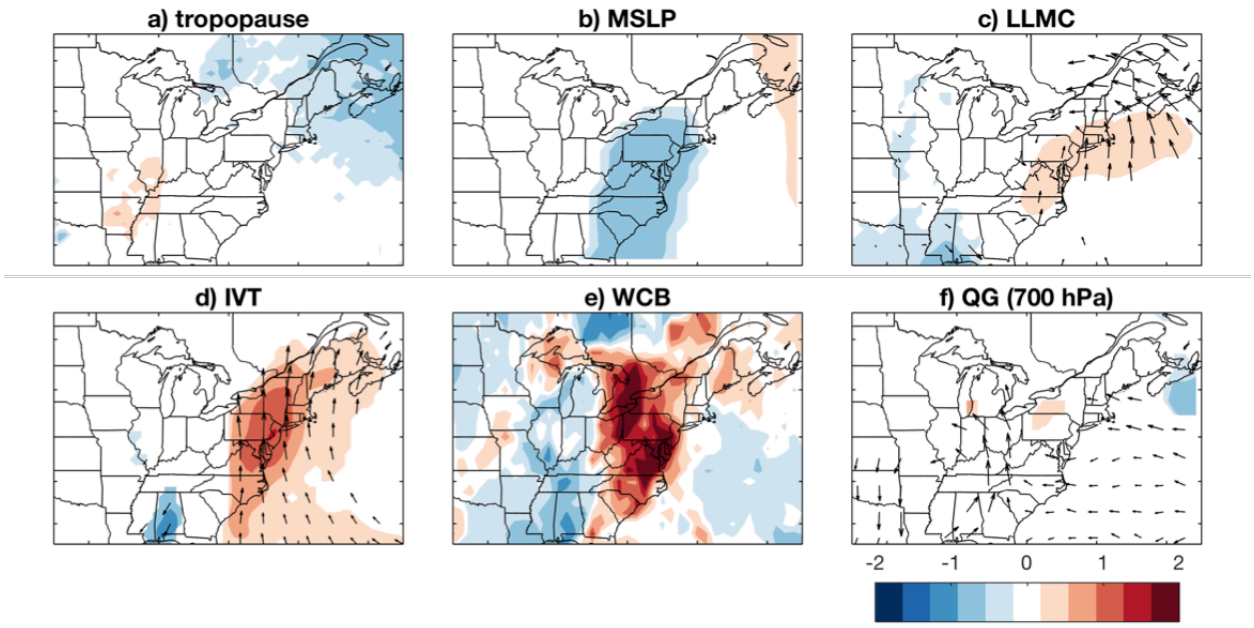

Fig. 14 Same as Fig. 9, but for SOM1 (similar to C6)

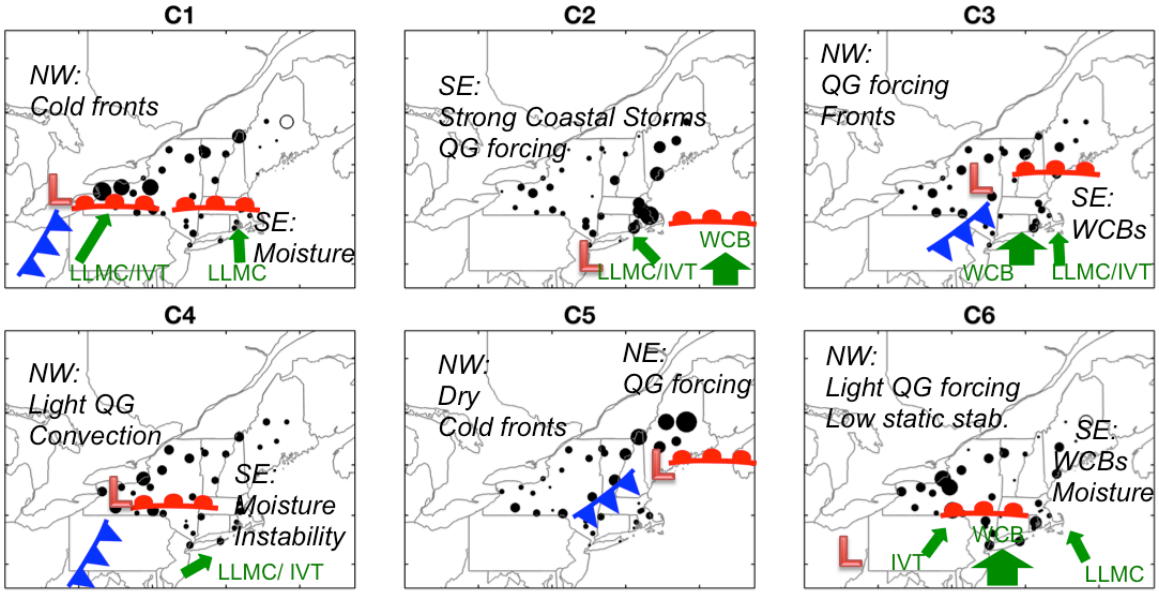

Fig. 15 Identification of key ingredients and processes linked to extreme precipitation for each of the k-means patterns C1–C6. Shown are dominant moisture processes (LLMC, IVT, WCBs; green arrows), cold fronts, warm fronts, and low pressure centers (orange L symbol), and station locations experiencing extremes (black dots, with size of dot indicating relative frequency of extremes within pattern)

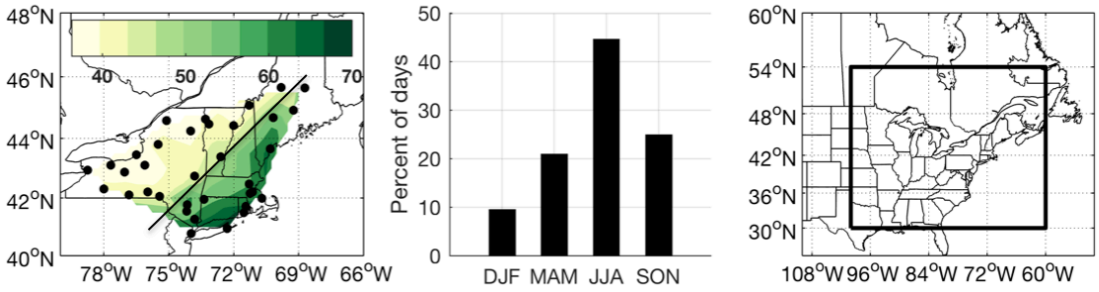

Fig. 1 Plots of (a) USHCN station locations (black dots) and top 1% daily precipitation thresholds interpolated from station locations (shaded, in mm), (b) seasonal frequency of top 1% extreme precipitation days excluding those due to tropical cyclones (shown as a percent of n=691 days), and (c) domain used for typing (bounded by thick black line). Top 1% thresholds based on wet-day precipitation, 1979-2008. Figure reproduced from Agel et al. (2017).

Reference:

Agel L, Barlow M, Feldstein SB, Gutowski WJ (2017) Identification of large-scale meteorological patterns associated with extreme precipitation in the US northeast. Climate Dynamics 1-21 doi:10.1007/s00382-017-3724-8

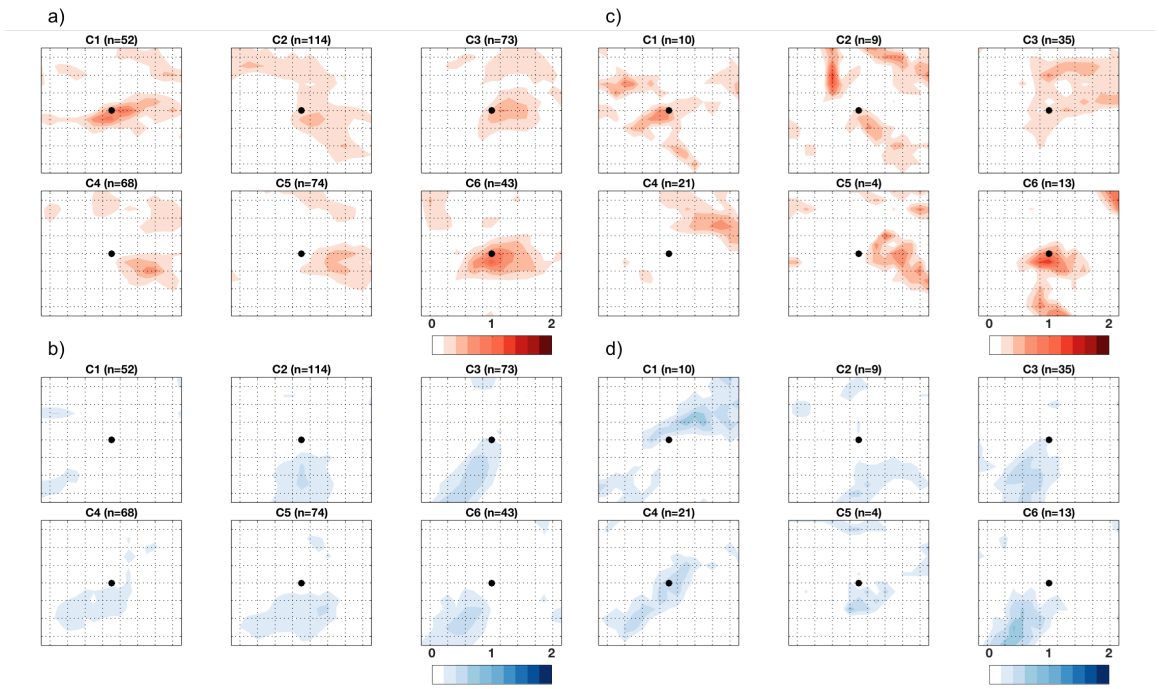

Fig. 1 Composite *coastal station* storm-related (when there are synoptic storm centers within 800 km of a station experiencing extreme precipitation) a) warm and b) cold frontal density; and composite *coastal station* non-storm-related (when there are no synoptic storm centers within 800 km of a station experiencing extreme precipitation) c) warm and d) cold frontal density for KMC pattern C1–C6 days. The frontal densities are calculated based on relative position to station location, with the station location shown in center (black dot) of 40° longitude x 36° latitude grid. The value following the pattern title above each frame represents the number of station-extremes included in the composite. Fronts based on Era-Interim reanalysis as in Catto et al. (2014).

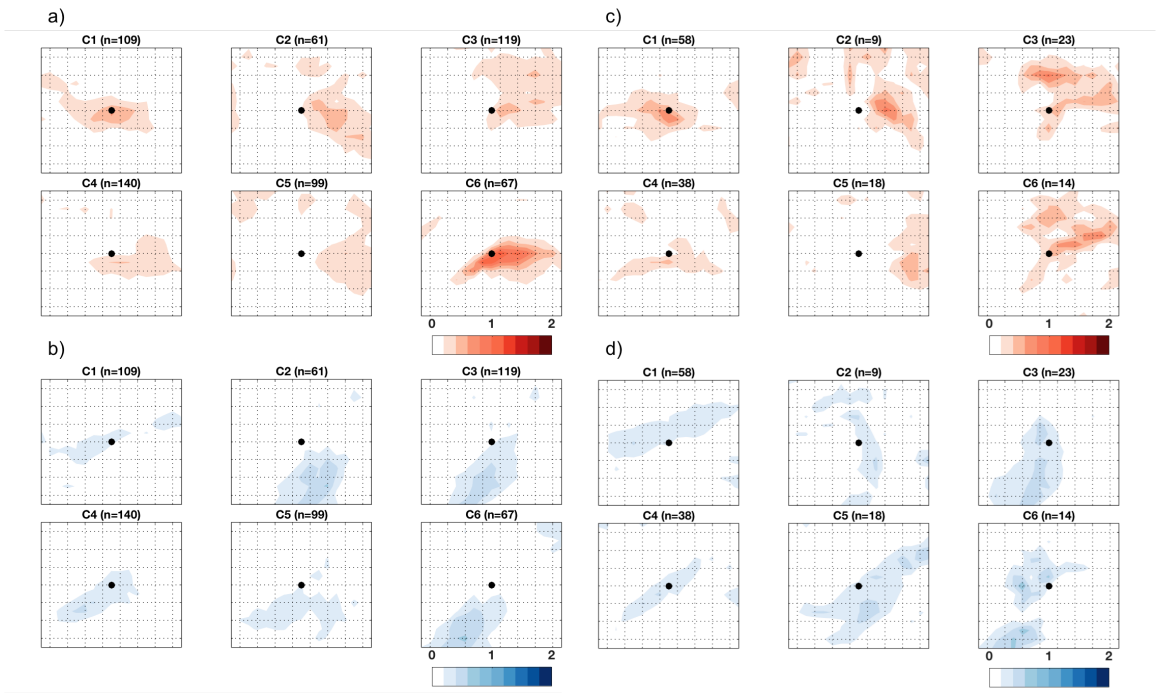

Fig. 2 Composite *inland station* storm-related (when there are synoptic storm centers within 800 km of a station experiencing extreme precipitation) a) warm and b) cold frontal density; and composite *inland station* non-storm-related (when there are no synoptic storm centers within 800 km of a station experiencing extreme precipitation) c) warm and d) cold frontal density for KMC pattern C1–C6 days. The frontal densities are calculated based on relative position to station location, with the station location shown in center (black dot) of 40° longitude x 36° latitude grid. The value following the pattern title above each frame represents the number of station-extremes included in the composite. Fronts based on Era-Interim reanalysis as in Catto et al. (2014).

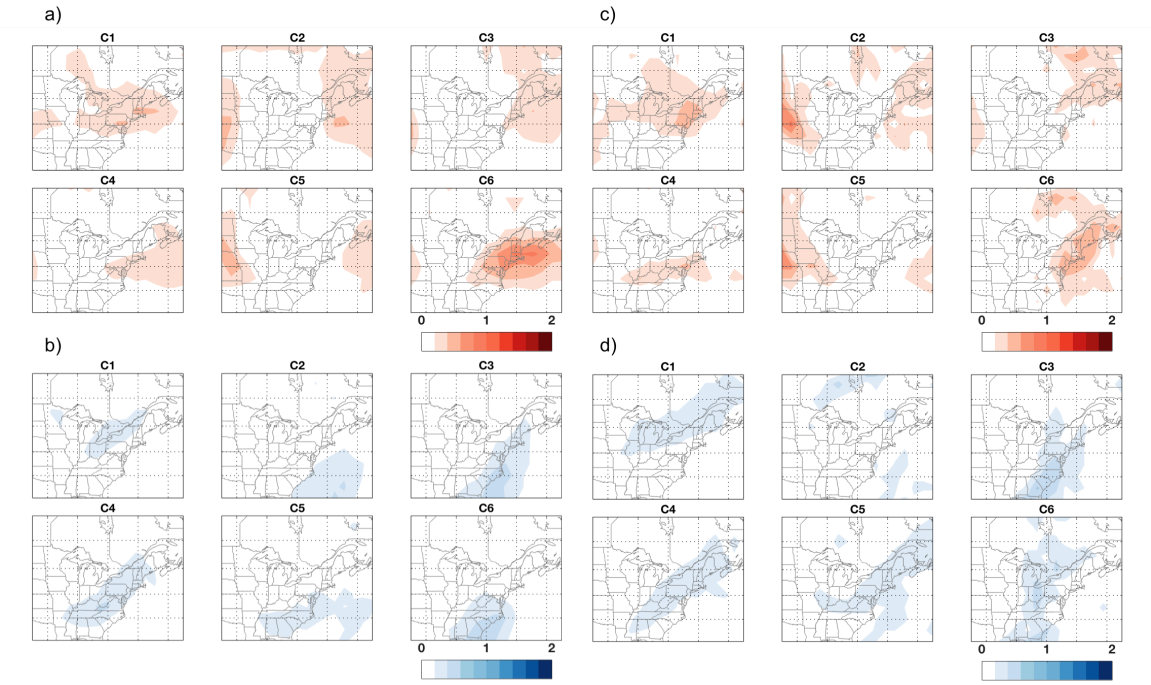

Fig. 3 Composite storm-related (when there are synoptic storm centers within 800 km of a station experiencing extreme precipitation) a) warm and b) cold frontal density; and composite non-storm-related (when there are no synoptic storm centers within 800 km of a station experiencing extreme precipitation) c) warm and d) cold frontal density for KMC pattern C1–C6 days. Fronts based on Era-Interim reanalysis as in Catto et al. (2014).

References:

Catto JL, Nicholls N, Jakob C, Shelton KL (2014) Atmospheric fronts in current and future climates Geophysical Research Letters 41:7642-7650 doi:10.1002/2014GL061943

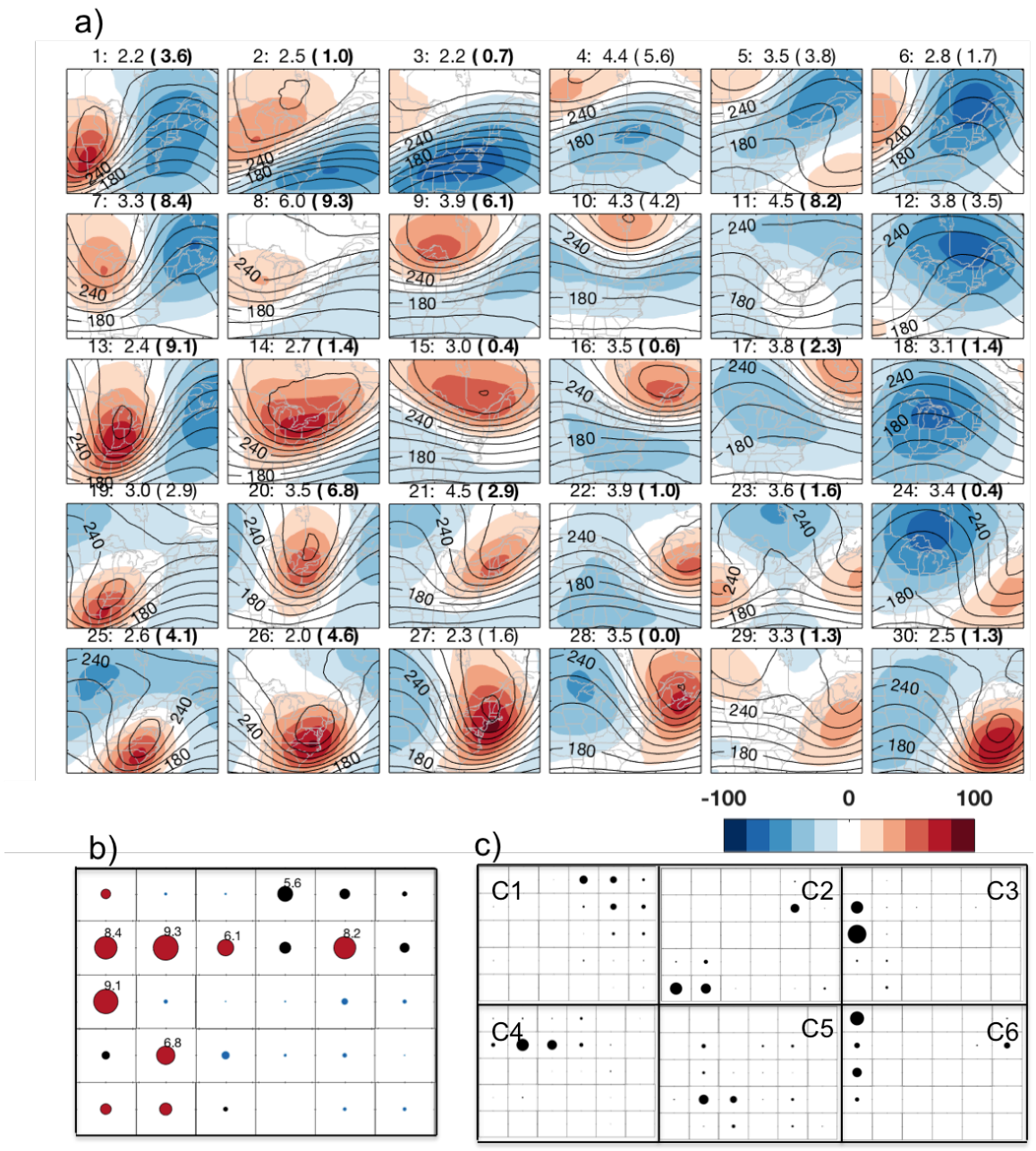

Fig. 1 This figure shows the (a) SOM separation of MERRA 1979-2008 daily tropopause pressure (contours, in 20 hPa intervals, and anomalies, shaded), separated into a 5 x 6 rectangular phase-space, (b) fraction of 691 top 1% extreme precipitation days represented by each SOM pattern, with size of circles proportional to values, and red, blue, and black circles indicating significantly higher, lower, or average, respectively, values than expected based on Monte Carlo resampling, and (c) fraction of KMC C1–C6 patterns represented by each SOM pattern, with size of circles proportional to values. Figure recreated from Agel et al. 2017.

Reference:

Agel L, Barlow M, Feldstein SB, Gutowski WJ (2017) Identification of large-scale meteorological patterns associated with extreme precipitation in the US northeast. Climate Dynamics 1-21 doi:10.1007/s00382-017-3724-8